Chapter 5
Effect of Pressure on Thermo-oxidation and Thermocatalytic Oxidation of *n*-C_7 Asphaltenes

Oscar E. Medina, Jaime Gallego, Farid B. Cortés, and Camilo A. Franco

5.1 Introduction

A mechanistic and kinetic/thermodynamic understanding of asphaltene oxidation is crucial for determining the thermal reaction pathway of heavy (HO) and extra-heavy (EHO) crude oils in thermal enhanced oil recovery (TEOR) applications [1]. These methods use the heat exchange for reducing oil viscosity and therefore improve their mobility inside the reservoir. Technologies that involve the injection of oxidizing agents such as air and oxygen are widely used worldwide, known as combustion process [2, 3]. Furthermore, these fluids are less expensive and require less economic investment than the injection of other fluids such as steam and non-condensable gases [4, 5]. Despite these advantages, some limitations are associated with the combustion front and coke formation in the reservoir due to the high temperatures in these technologies [6]. Asphaltenes are the primary sources of coke [7]. Their composition of aliphatic chains surrounding aromatic rings makes them atypical structures, that once they lose the structures around them, they become more refractory, more condensable, and more massive [8]. Asphaltenes' thermal behavior is of great interest due to their coking tendency and catalyst deactivation during the injection of hot gases, mainly air or oxygen-rich fluids [9, 10]. Because of these

O. E. Medina · F. B. Cortés (✉) · C. A. Franco (✉)
Grupo de Investigación en Fenómenos de Superficie–Michael Polanyi, Departamento de Química y Petróleos, Facultad de Minas, Universidad Nacional de Colombia Sede Medellín, Medellín, Colombia
e-mail: oemedinae@unal.edu.co; fbcortes@unal.edu.co; caafrancoar@unal.edu.co

J. Gallego
Química de Recursos Energéticos y Medio Ambiente, Instituto de Química, Universidad de Antioquia UdeA, Medellín, Colombia
e-mail: andres.gallego@udea.edu.co

N. N. Nassar et al. (eds.), *Nanoparticles: An Emerging Technology for Oil Production and Processing Applications*, Lecture Notes in Nanoscale Science and Technology, https://doi.org/10.1007/978-3-319-12051-5_5

molecules' complexity, nanotechnology has been employed by several authors to improve the kinetic oxidation rate and reduce the energy required for the thermal asphaltene decomposition [11–13]. By evaluating different chemical natures of nanoparticles, it has been identified that its phase complexity is imperative for selective oxidation of asphaltenes [14–16]. Besides, the compensation effect can help understand the chemical reaction pathway during this process.

Nevertheless, there are no studies in the specialized literature that report the effect of pressure and compensation effect of asphaltene thermo-oxidation and thermocatalytic oxidation. In this sense, this research opens a new landscape on the oxidative behavior of the heaviest fractions of crude oil under the reservoir and in situ combustion conditions, providing the first insights in this area.

This chapter summarizes the main results obtained after robust research on the effect of pressure on nanotechnology-assisted oxidative phenomena. The topics include (*i*) advantages and disadvantages of the main thermal recovery methods; (*ii*) application of nanotechnology in low-pressure asphaltene reaction kinetics; (*iii*) theoretical insights about thermodynamic compensation effect; (*iv*) characterization of seven different *n*-C_7 asphaltenes; (*v*) synthesis and characterization of novel nanocatalysts; (*vi*) adsorption and modeling of asphaltenes on nanocatalysts; (*vii*) high-pressure thermogravimetric experiments on virgin asphaltenes, effect of pressure, and their chemical nature; (*viii*) thermocatalytic oxidation of asphaltenes at different pressures in the presence of various nanocatalysts; (*ix*) kinetic analysis based on effective activation energy and Arrhenius pre-exponential factor; and (*x*) discussion of the thermodynamic compensation effect. Eventually, this study leads to the elucidation of the asphaltene decomposition pathways in an oxidizing atmosphere and, therefore, a better understanding of EOR processes' improvement through nanotechnology.

5.2 Thermal Enhanced Oil Recovery Processes

Enhanced oil recovery (EOR) methods are used in the oil and gas industry for increasing the productive life of crude oil reservoirs [17]. Since 1950, for the production of heavy (HO) and extra-heavy crude oils (EHO), thermal (TEOR) processes are commonly used [18] to supply heat into the reservoir and vaporize part of the crude oil [19]. TEOR methods use the temperature as a tool to improve HO and EHO mobility by oil viscosity reduction. During the heating process, thermal expansion of rock and fluids, variation in capillary pressure, the volatilization of light hydrocarbons, and gravitational segregation occur. TEOR includes hot water injection, steam injection, in situ combustion, and electric heating [2, 3].

Steam is injected into the reservoir in different ways including cyclic steam injection (CSS), continuous steam injection, and steam-assisted gravity drainage (SAGD).

CSS also called Huff and Puff involves several steam injection periods for heating the reservoir in the near-wellbore area, using a single well that functions as an

injector for steam and producer for crude oil. Precisely, CSS consists of three main stages including (*i*) steam injection into the reservoir; (*ii*) soaking time, where the well is closed to production for heat exchange; and (*iii*) production time, where the well is opened for HO and EHO production. In the soaking period, the crude oil is heated, and its viscosity decreases [20]. Temperatures of around 200°C to 300°C are reached, and production rates remain high for a short time before decreasing. The steam-to-oil ratio increases as cycles progress, leading to decreased economic gain. A good design of the technique is necessary to achieve high productivity; this factor must consider permeability, oil viscosity, and injection depth [21, 22]. Approximately 30% of OOIP is recovered with CSS [23, 24].

Continuous steam injection is used as a recovery technique to extract denser crude oils and began around 1960 in California to complement recovery by cyclical steam injection [25]. A continuous heat supply by steam is required, and it is realized in the injection wells, so that the steam advances in the reservoir, transferring heat and decreasing the oil's viscosity. As the steam front progresses, steam condensation builds up, helping move crude oil to the producing wells. With this technique, 50% of the OOIP is recovered [26, 27]. Like cyclical steam injection, steam injection faces several economic and environmental challenges related to CO_2 emissions during steam generation. The steam generation water has problems such as handling large amounts of liquid and an additional dehydration facility for the separation of the generated emulsions [28].

Steam-assisted gravity drainage (SAGD) is a technique applied mainly to extra-heavy crudes and oil sands. It was invented by Dr. Roger Butler in Canada in 1970 due to the high viscosity of hydrocarbons in that country [29, 30]. SAGD is currently one of the most efficient recovery methods that achieve recoveries up to 70% of OOIP along with high production rates [31, 32]. The technique consists of drilling two horizontal wells, placing one at 4 m–6 m above the other. Steam is injected into the upper well to heat the crude oil, reduce its viscosity, and promote its movement to the lower well (production well). Injected steam creates a steam chamber that continuously expands to push condensed water and heated oil into the producing well. This technique's application is restricted by several factors, including geological environment, reservoir thickness, vertical and horizontal homogeneity, and high permeability.

Furthermore, the presence of gas and an aquifer can reduce the efficiency of the technique [33, 34]. On the other hand, the high volumes of water involved in steam generation and gas consumption as fuel can cause high costs. To solve these problems, variations on the technique have been proposed, such as chemical solvents and non-condensable gases [4, 5].

In situ combustion, the heat is generated in the reservoir by igniting a part of the crude oil. During the injection of fluids, surface heat is generated and transferred to the reservoir. Water is one of the generally used fluids, which can be injected as hot water or as steam [25, 35]. The methods of thermal recovery can be used in both horizontal and vertical wells. However, generally in horizontal wells, its application can be more complex and expensive. In horizontal wells, techniques such as expanded solvent with gravity drainage (ES-SAGD), vapor extraction (VAPEX),

and SAGD are used to improve the sweep efficiency, increase the contact area, and oil rate production [17].

In situ combustion is generated by injecting air or oxygen to ignite a small portion of the oil in the reservoir, reaching temperatures between 450°C and 600°C. Because heat originates in situ, heat losses are minimum, making it an efficient method [36, 37]. Exothermic oxidation reactions release a high amount of heat that helps improve the mobility of heavy oil, burning a small part. There are three methods of in situ combustion: (*i*) frontal combustion, where the ignition is generated near to the injector well and the hot zone advances in production direction; (*ii*) reverse combustion, where the front combustion advances in the opposite direction of airflow, and (*iii*) high-pressure air injection. This process does not involve recycling water and has a very low emission of gases. Therefore, it is the most crucial technique for exploiting heavy and extra-heavy crude oils [38].

The process begins with ignition, where a gas chamber consisting of air and flue gases forms at the combustion front. Through the combustion front propagation, continuous expansion of the gas chamber is generated, which helps to move the unburned oil towards the production wells [6]. The in situ combustion mechanism is described by well-defined zones, including the burned, combustion, cracking, evaporation, and steam area. These areas are characterized by having different temperatures and different saturations of oil and water [39, 40]. However, despite the many benefits that this technique offers, several limitations must be overcome, and that is not yet fully understood [41]. There is still no adequate control of the combustion front and the portion of burned oil or its heating rate. Furthermore, the primary sources of coke are asphaltenes, and to date, no studies of its oxidative behavior under reservoir conditions have been dated. Understanding these mechanisms and finding technologies that improve these fractions' reactivity could improve the efficiency of these technologies since many operations could be optimized to obtain a higher recovery factor.

5.3 Nanocatalysts for Asphaltene Decomposition and Heavy Oil Upgrading

In recent decades, nanotechnology has emerged as an innovative technology applicable to the oil and gas industry, especially in the remediation and inhibition of formation damage and potentializing EOR processes [42]. By convention, nanoparticles are in the range of 1 nm−100 nm. Their size and unique characteristics make them suitable for application in porous media [43]. Among nanoparticles' properties are their high surface area-to-volume ratio, their selectivity towards heavy components of crude oil, their unique optical and chemical characteristics, and the presence of active surfaces [44, 45].

The production of heavy and extra-heavy crudes is a challenge that the industry faces every day due to the high viscosity and low mobility. Thermal recovery

methods have proven to be very efficient in increasing the production of this type of hydrocarbon [18]. The increase in temperature and the injection of heat can occur in situ or through some fluid. This provides better sweep efficiency and an increase in recovery factor with decreased viscosity [22].

A synergy between nanotechnology and thermal recovery methods has emerged as an alternative to increase hydrocarbon production. In recent years, several studies have focused on the synthesis and development of catalytic nanoparticles that reduce the decomposition temperature of asphaltenes and resins, taking advantage of the temperatures generated by thermal recovery processes. Different materials have been employed, including non-functionalized and functionalized nanoparticles as mono- [46] and multi-elemental oxides [46, 47] for the asphaltene catalytic decomposition and HO and EHO upgrading [48]. Among the most recent studies, it has been employed nanocatalysts of SiO_2 [16, 49], TiO_2 [47], CeO_2 [50–52], and Al_2O_3 [47, 53, 54] resulting in significant reductions in the decomposition temperatures of asphaltenes in different atmospheres (air, steam, inert).

To evaluate the catalytic capacity of nanoparticles, low-pressure thermogravimetric analysis and differential scanning calorimetry (DSC) are commonly used. Among the first applications of nanoparticles for the oxidation of asphaltenes, Nassar et al. [55] investigated the adsorption and subsequent oxidation of Athabasca asphaltenes in different metal nanoparticles (NiO, Co_3O_4, and Fe_3O_4) [55]. The authors found reductions of more than 100°C in the asphaltene decomposition temperature in all cases, obtaining a better result for NiO nanoparticles. Furthermore, the surface acidity of the nanoparticles was evaluated in another study [56]. Basic, acid, and neutral alumina were assessed for the oxidation of Athabasca asphaltenes. The results show affinity increases as the acidic surface increases. On the contrary, catalytic activity is higher for basic alumina.

Besides, Fe_3O_4 nanoparticles were used for catalytic oxidation of different visbroken asphaltenes from a cracked vacuum residue. Results show a significant reduction in the oxidation temperature and average activation energy [57]. Also, TiO2, ZrO2, and CeO2 nanoparticles' catalytic activity has been investigated [58]. CeO_2 nanoparticles showed the highest performance for asphaltene catalytic oxidation, confirmed by the lowest effective activation energy trends and lowest values of Gibbs free energy and enthalpy changes.

On the other hand, fumed silica nanoparticles were functionalized with transition element oxides of Ni and Pd at different dosages for the oxidation of Colombian asphaltenes [16]. This study presents essential conclusions on the application of functionalized materials. First, a higher dosage of each metal in the mono-elemental nanoparticles increases the catalytic capacity of the material. Also, bi-elemental nanoparticles show better performance than mono-elemental nanoparticles. The application of transition elements can significantly improve the performance of TEOs, and the application of design of experiments can lead to the development of an optimal material to reduce the activation energy for the catalytic oxidation of asphaltenes, which has a dosage of 0.29% Ni and 1.32% Pd on the surface of the nanoparticle.

The influence of resins on the adsorption of asphaltenes on nanoparticles has also been studied. The results present different adsorption isotherm types according to the resin/asphaltene ratio. It was concluded that resins I do not significantly influence asphaltene adsorption on nanoparticles and help to solubilize in the medium [59]. Other works have focused on the effect of resins I on the catalytic decomposition of asphaltenes adsorbed on nanoparticles. A combined method of thermogravimetric analysis and softening point measurements was used to evaluate the adsorption of asphaltenes and resins I in heavy oil model solutions. The results of the catalytic behavior show that the presence of resins I do not significantly change the decomposition temperature of the asphaltenes adsorbed on the nanoparticles. However, the catalytic effect of the nanoparticles is affected by an increase in activation energy as the presence of resins increases in the system [60].

Despite all efforts to understand and optimize TEOR methods by nanotechnology application, the effect of pressure on the interaction of isolated asphaltene molecules and nanoparticles has not yet been reported in the literature. All these investigations have been evaluated at atmospheric pressure, without considering the high pressures to which the crude oils may be subjected in the reservoir and in situ combustion processes. The few works carried out under reservoir conditions directly evaluate the matrix of HO and EHO. Still, to optimize these processes, it is important to understand how the individual fractions behave, specifically the coke precursors in the reservoir, in nanoparticles' absence and presence.

5.4 Compensation Effect

Essentially, the rate of all thermally activated processes is described by the Arrhenius law, where the rate r is temperature-dependent, following the expression $r(T) = k_o e - E_a^{app} / k_B T$, where, k_B is the Boltzmann's constant. Kinetic parameters (E_a^{app} and k_o) determine the temperature dependence and overall rate, respectively, during thermal processes. Experimental studies have shown that in some systems, by varying E_a^{app} values, a thermodynamic compensation effect is reflected in k_o changes. A direct relationship between both parameters was found, described by Eq. (5.1)

$$\ln(k_o) = aE_a^{app} + b \tag{5.1}$$

The kinetic parameters characterizing the system, according to Eq. (X), are linearly related to E_a^{app} as a function of $\ln(k_o)$. The term "compensation effect" was introduced in 1908 by Wilson et al., by evaluating the electron emission phenomenon on a heated platinum surface in a hydrogen environment. Later, the compensation effect was used in catalysis processes, and it has been found that it is valid for a large number of homogeneous and heterogeneous chemical reactions. Since then, the compensation effect has been used to study thermal and nonthermal processes'

reaction mechanisms, including bulk diffusion, polymer dielectric relaxation, and electrical conduction, among others. In thermal reactions, the compensation effect is known as isokinetic relationship because the linear dependence of Eq. (5.1) leads to an isokinetic temperature ($T_{isokinetic}$) expressed by the slope of the line. This temperature implies that all the considered reactions have the same rate. However, $T_{isokinetic}$ is often outside the range of experimentally accessible reaction conditions. Commonly, the compensation effect of chemical reactions leads to real compensation in the rate, considering the values for a always positive. Nevertheless, despite the majority of the cases, there are a large of chemical processes that have negative values for a.

Despite many attempts to explain the compensation effect in different processes, the term is not universally accepted, arguing that the nature of Arrhenius's law is such that the experimental determination of kinetic parameters is associated with large statistical uncertainties which rise to a compensatory effect.

On the other hand, the compensation effect can be distinguishable and categorized according to the nature and range of the reactants and/or reaction conditions, together with the common constant and systematically modified features. The type I compensation effect for heterogeneous reactions is associated with modification of the chemical reaction or the catalysts. Type II represents the compensation effect for experimental condition variation (i.e., pressure, temperature, heating rate), and type III is associated with practical calculation changes. That is, the estimation of kinetic parameters is realized using different computational programs or different rate equations.

In this order, in this work, we will show that for a broad class of experimental conditions and catalysts with different active site distributions, the compensation effect can be explained. First, the type II compensation effect will be demonstrated by pressure changes during asphaltene oxidation in nanocatalysts' presence and absence. Then, the type I compensation effect will be explained using a different class of nanocatalysts.

5.5 Materials and Methods

5.5.1 Materials

5.5.1.1 Nanoparticles and N-C_7 Asphaltenes

Ceria-zirconia mixed oxide ($Ce_{0.62}Zr_{0.38}O_2$) as support and impregnated with Au and Pd noble oxides in 3:1 and 10:1 Au/Pd initial nominal molar ratios was used for asphaltene adsorption and subsequent catalytic oxidation. Nanocatalysts were synthesized by deposition-precipitation of Au followed by incipient wetness impregnation of Pd. Details of the synthesis procedure are found in our previous work [1]. The surface area (S_{BET}) of bi-elemental catalysts and support was $67\ m^2 \cdot g^{-1} \pm 2\ m^2 \cdot g^{-1}$. The final load of element oxides on surface support was determined by inductive

coupled plasma-atomic emission spectrometry (ICP-AES). Results demonstrate that the nominal molar ratio remains equal to 3:1 and 10:1 at the end of the synthesis process. According to the Au/Pd nominal molar ratio, functionalized nanocatalysts were named as 3:1AuPd and 10:1AuPd.

Also, STEM-XEDS analysis corroborates the formation of metallic particles in functionalized nanocatalysts. The crystal size of Au and Pd varies between 1 and 5 nm and the respective dispersions near to 36%, for both systems. Finally, by X-ray photoelectron spectroscopy, the main functional groups of each catalyst were obtained. These results are summarized in Table 5.1.

Initially, a single asphaltene source was used to evaluate the effect of pressure on its oxidation in the absence and presence of nanocatalysts. Then, six different asphaltenes were obtained from different HO and EHO around the world to address the chemical nature effect on reactivity at low- and high-pressure conditions. Asphaltene isolation was done by mixing *n*-heptane (99%, Sigma-Aldrich, St. Louis, MO) with the HO following the protocol described in the standard ASTM D2892 and ASTM D5236 [62–64]. The samples were characterized by elemental analysis (EA) estimated using a Thermo Flash elemental analyzer EA 1112 (Thermo Finnigan, Milan, Italy) to determine the C, H, S, O, and N content, following the protocol described in previous works [65]. The average molecular weight was estimated using a Knauer osmometer (Knauer, Berlin-Heidelberg, West Germany) calibrated with benzyl and using the steps enlisted in literature [66]. X-ray photoelectron spectrometry was performed on a Specs brand X-ray photoelectronic spectrometer (NAP-XPS) with a PHOIBOS 150 1D-DLD analyzer, using a monochromatic source of Al-Kα (1486.7 eV, 13 kV, 100 W) with step energy 90 eV and 20 eV for general and high-resolution spectra, respectively. Finally, ^{1}H NMR and ^{13}CNM were developed on a Bruker AMX 300 spectrometer (Karlsruhe, Germany) operating at 300 MHz, with a 5 mm inner diameter tube. The samples were dissolved in $CDCL_3$ (99.8%) containing traces of tetramethylsilane (TMS) used as standard internal solvents. Details of the procedure are found in a previous study [67]. Considering the results of EA, VPO, and ^{13}CNM, average molecule construction was done using Materials Studio (BOVIA, San Diego, CA, USA), following the Lee-Yang-Parr function and Clar's theory [68, 69].

Table 5.1 Superficial atomic content (%) of Ce, Au (4f signal), and Pd (3d signal) ions through XPS of bi-elemental catalysts supported on $Ce_{0.62}Zr_{0.38}O_{2\pm\delta}$

Catalyst	Ce3+ (atomic %)	Au^0 (atomic %)	$Au^{\delta+}$ (atomic %)	Pd^0 (atomic %)	Pd^{2+} (atomic %)
3:1AuPd[a]	20	100	0	37.7	62.3
10:1AuPd[a]	34	100	0	50.4	49.6

[a]Results acquired from previous work [61]

5.5.2 Methods

5.5.2.1 Adsorption Isotherms

The amount of asphaltenes adsorbed on the different nanocatalysts was determined by a colorimetric method using a UV-vis spectrophotometer Genesys 10S UV-VIS (Thermo Scientific, Waltham, MA, USA) at a wavelength fixed at 295 nm [70, 71]. Asphaltene initial concentrations were varied between 100 mg·L^{-1} and 1500 mg·L^{-1}. Besides, the toluene was used as a blank in the calibration curve and as an agent for dilution [72].

The procedure starts by adding the constant mass of nanoparticles to the prepared heavy oil model solutions in a ratio of 1:10 mass/volume. This solution to nanoparticles ratio is used to allow the adsorbent decantation for the UV-vis absorbance measurements. All samples were mixed at 200 rpm for 24 h at 25°C to ensure the equilibrium, unless otherwise specified. Then, by centrifugation, the nanoparticles containing asphaltenes were separated. Runs were done by triplicate, obtaining a deviation of 0.05 mg·L^{-1}. The amount of n-C_7 asphaltenes adsorbed "q" is calculated using the mass balance in Eq. (5.2)

$$q = \frac{\left(C_0 - C_E\right) \cdot M}{A} \tag{5.2}$$

where C_E (mg·L^{-1}) represents the n-C_7 asphaltene concentration in the equilibrium, M (L·g^{-1}) is the solution volume/nanoparticle mass ratio, and A (m^2·g^{-1}) denotes the surface area of the adsorbent.

5.5.2.2 Kinetic Study by High-Pressure Thermogravimetric Analysis

Kinetic analysis of n-C_7 asphaltenes oxidation assisted by nanocatalysts was carried out using a high-pressure thermogravimetric analyzer 750 (TA Instruments, Inc., Hüllhorst, Germany). The equipment operates with a uniform electromagnetic field generated by a magnetically levitated balance. Figure 5.1 shows a diagram of the gas supply system for the equipment. It comprises four gas mass flow controllers (MFCs) to guarantee a correct flow of the working gas at different pressures. Initially, the sample surface is cleaned under a vacuum at 0.00025 MPa for 10 min by N_2 injection at 5 mL·min^{-1}. Then, two runs are done at the same operation conditions due to flow effects, one for the sample to analyze and the other for the empty sample holder. Automatic correction is made by subtraction of the respective measurements.

Non-isothermal experiments were executed at different heating rates of 5°C·min^{-1}, 10°C·min^{-1}, and 15°C·min^{-1}. Air injection was done by a flow of 80 mL·min^{-1}, and the mass was fixed in 1 mg to avoid mass and heat diffusional effects [1, 73]. Thermal experiments were developed in three main subsections that

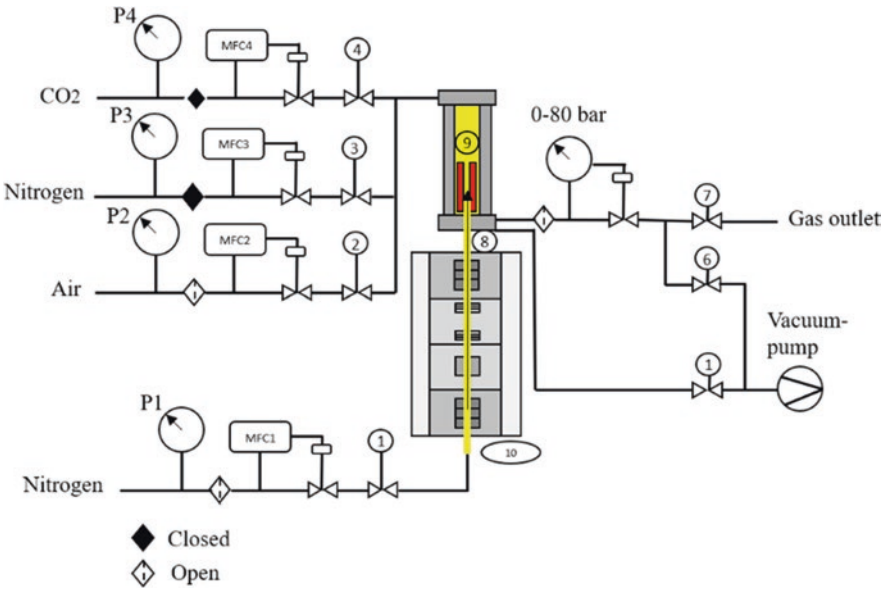

Fig. 5.1 Representative diagram for the gas supply system of the HP-TGA 750. (MCF# corresponds to gas mass flow controllers, P# the manometers, 1–6 are the automatic valves, 7 is the gas outlet pressure regulator, 8 is the tube balance, 9 is magnet levitated balance, and 10 is the high-pressure reaction furnace)

involve (*i*) virgin *n*-C_7 asphaltene oxidation for a single source in a wide range of pressures between 0.084 MPa and 7.0 MPa, (*ii*) oxidation of different sources of *n*-C_7 asphaltenes at low- and high-pressures, and (*iii*) oxidation of nanocatalysts containing *n*-C_7 asphaltenes.

5.6 Modeling

5.6.1 Solid-Liquid Equilibrium Model

This model, from the theory of adsorption and association of molecules over microporous surfaces [74], describes the adsorption and desorption isotherms using the following equations (Eqs. 5.3, 5.4 and 5.5).

$$C = \frac{\psi H}{1 + K\psi} e^{\left(\frac{\psi}{Q_m A}\right)} \tag{5.3}$$

$$K = \frac{K_T RT}{SA} \tag{5.4}$$

$$\psi = \frac{-1+\sqrt{1+4K\xi}}{2K} \tag{5.5}$$

where the concentration of asphaltenes in the equilibrium is represented by C ($mg \cdot g^{-1}$) and H ($mg \cdot g^{-1}$) refers to the affinity between the adsorbate-adsorbent couple. Similarly, K ($g \cdot g^{-1}$) indicates the self-association degree of n-C_7 asphaltenes on nanoparticles, and Q_m ($g \cdot g^{-1}$) is the maximum adsorption capacity of nanoparticles [75].

5.6.2 Activation Energy Estimation

Estimation of kinetic parameters (i.e., Arrhenius pre-exponential factor and activation energy) was done using a single power law equation bearing in mind the immediate reactivity of the materials. Ozawa-Wall-Flynn approximation was used to resolve non-isothermal experiments [76], leading the Eq. (5.6):

$$\ln\left[\frac{\beta F(\theta)}{P_{O_2}^n T^2}\right] = \ln\left(\frac{k_o R}{E_a}\right) - \frac{E_a}{RT} \tag{5.6}$$

where β ($°C \cdot min^{-1}$) is the heating rate, **P** (bar) is the oxygen partial pressure, n represents the order of oxidation reaction, E_a ($kJ \cdot mol^{-1}$) is the effective activation energy, k_o ($s^{-1} \cdot bar^n$) is the Arrhenius pre-exponential factor, and R ($J \cdot mol^{-1} \cdot K^{-1}$) is the ideal gas constant. Besides, $F(\theta)$ is represented by the expression ($\int d\theta / f(\theta) = -\ln(1-x)$) related to the volumetric consumption model [1, 73].

5.7 Results

5.7.1 Characterization of N-C_7 Asphaltenes

The elemental composition and average molecular weight results of the asphaltene samples are shown in Table 5.2. Carbon content varies between 81.0% and 85.0% while hydrogen content between 7.1% and 7.8%. Differences in heteroatom content between each sample were observed. The atomic percentage for nitrogen increases in the order SS < C < A ≈ D < E < F < B. Particularly, SS sample has a content below to 0.5%. Sulfur content is the predominant heteroatom in all samples, for values higher than 3.9%. Finally, oxygen content varies between 2.9% and 3.6%. On the other side, molecular weight increases in the order E < F < C < D < SS < A < B, according to the different elemental composition in each sample. A complete analysis is reported in a previous work [67].

Table 5.2 Elemental composition and average molecular weight of n-C_7 asphaltenes of different sources

Sample	Elemental mass fraction concentration ± 0.2%					M_W ± 5.0 g·mol^{-1}
	C	H	N	S	O	
SS	81.7	7.8	0.3	6.6	3.6	907.3
A[a]	82.6	7.3	1.5	5.4	3.2	950.3
B[a]	81.9	7.7	1.9	5.3	3.2	1051.6
C[a]	82.5	7.7	1.1	5.3	3.4	722.4
D[a]	83.0	7.2	1.5	5.4	2.9	717.3
E[a]	84.7	7.2	1.6	3.5	3.0	555.7
F[a]	84.3	7.1	1.8	3.9	2.9	650.9

[a]Results acquired from previous work [67]

Table 5.3 Carbon types present in whole n-C_7 asphaltenes and its fractions obtained by ^{13}C-NMR analysis

Carbon		Relative amount (%) in asphaltenes					
	SS	A[a]	B[a]	C[a]	D[a]	E[a]	F[a]
C_{ar}	64.48	62.12	68.2	65.9	60.3	55.6	57.8
C_{al}	35.51	37.9	31.8	34.1	39.7	44.4	42.2

[a]Results acquired from previous work [67]

Carbon type proton distribution was obtained by the combination of normalization and integration processes of the ^{13}C NMR patterns and are shown in Table 5.3. The carbon was divided into two important regions, one for the aliphatic carbon content and the other for the aromatic carbon. The former increases in the order B < C < SS < A < D < F < E, while aromatic content follows the opposite behavior.

According to the NMR spectral analysis results, combined with elemental analysis and average molecular weight (VPO), asphaltene molecules were computationally resolved and are shown in Fig. 5.2 a–g. For all samples, island structure type adjusts correctly the experimental results obtaining theoretical molecular weights of 903.1 g·mol^{-1}, 959 g·mol^{-1}, 1043 g·mol^{-1}, 724 g·mol^{-1}, 701 g·mol^{-1}, 570 g·mol^{-1}, and 660 g·mol^{-1} for SS, A, B, C, D, E, and F samples, respectively. These are deviations lower than 3.0% for all asphaltenes. Molecular formulas are also enlisted in each figure. Results demonstrate that structural and chemical differences exist in each sample evaluated.

5.7.2 Adsorption Isotherms

Adsorption isotherms for SS asphaltenes over nanocatalysts are shown in Fig. 5.3. According to the International Union of Pure and Applied Chemistry (IUPAC) [77], this isotherm type is characterized by a high affinity between the adsorbent-adsorbate couple. For a fixed asphaltene concentration, adsorption amount increases

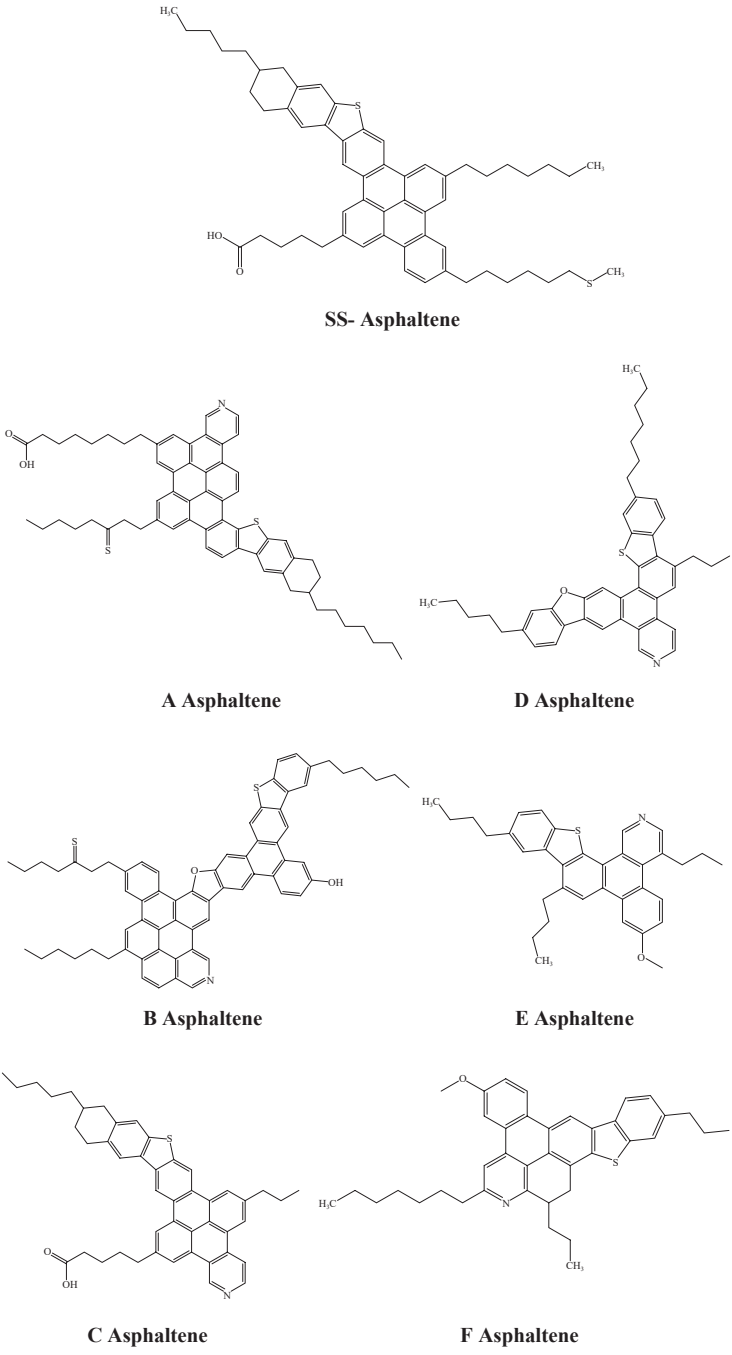

Fig. 5.2 Representative chemical structures for n-C_7 asphaltene samples constructed from results of NMR, elemental analysis, and average molecular weight. (Reproduced from Medina et al. [67] with permission)

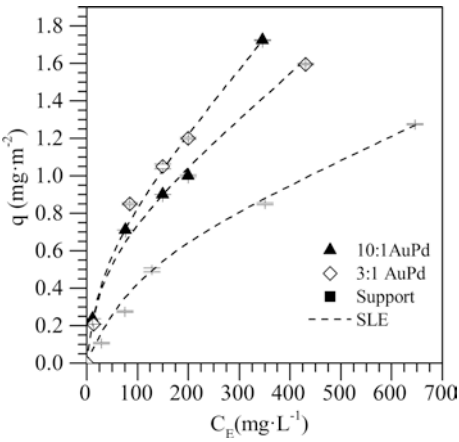

Fig. 5.3 *n*-C_7 asphaltene adsorption isotherms over support and functionalized nanocatalysts with different Au/Pd nominal molar ratios (3:1, and 10:1). (Taken with permission from Medina et al. [83])

in the order Support <3:1AuPd < 10:1AuPd. This trend is met throughout the range of concentrations evaluated. In the first instance, $Ce_xZr_{1-x}O_2$ mixed oxides show a high capacity for asphaltene uptake due to the affinity for the polyaromatic condensed structures for Ce^{3+} ions [50]. In addition, Zr^{4+} ions provide a higher capability to support by increasing the number of active sites for asphaltene adsorption and acid surface degree [78].

The incorporation of Au and Pd crystals improves the adsorption capacity and affinity according to the slope in Henry's region. Between both nanocatalysts, a nominal molar ratio of 10:1 shows a better performance than 3:1. According to XPS analysis, 10:1AuPd has a higher content of Pd0 ions, which can result in stronger chemical bonds with asphaltene molecules [79]. As was mentioned, Ce^{3+} plays a critical role in adsorption processes and is present in a higher load for 10:1 nanocatalyst [51]. These findings reveal that a heterogeneity surface is a key factor in increasing asphaltene adsorption, creating different selectivities for the nitrogen, oxygen, and sulfur functional groups of asphaltene structure. Compared with the literature, this study's selected nanocatalysts show a better performance [80–82].

5.7.3 High-Pressure Thermogravimetric Analysis

5.7.3.1 Effect of Pressure on N-C_7 Asphaltene Oxidation

Figure 5.4 shows the mass change and temperature profiles as a function of time for *n*-C_7 asphaltene oxidation at 6.0 MPa. This system was selected to illustrate the asphaltene oxidation behavior at high-pressure conditions. According to the mass change profile, the temperature was divided into four defined regions. The first region, named *oxygen chemisorption region* (OC), corresponds to the interval where an increase in asphaltene mass is observed, associated with incorporating oxygen atoms on its chemical structure from the oxygen-rich environment. The second

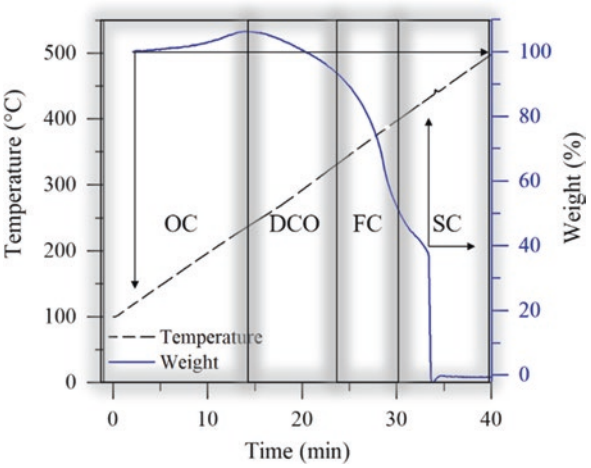

Fig. 5.4 Profiles for mass change and temperature for n-C_7 asphaltene oxidation at 6.0 MPa discretized in the four regions: (*i*) oxygen chemisorption (OC) region, (*ii*) decomposition of the chemisorbed oxygen (DCO) region, (*iii*) first combustion (FC) region, and (*iv*) second combustion (SC) region. Heating rate, 10°C·min^{-1}; airflow, 80 mL·min^{-1}; and sample mass, 6 mg. (Taken with permission from Medina et al. [73])

region, known as *decomposition of chemisorbed oxygen region* (DCO), is the temperature interval where the first decomposition and desorption of oxygenated compounds occurs, i.e., where mass sample begins its reduction. In this region, it also can occur the loss of lower molecular weight hydrocarbons and heteroatoms located in the branched structures. Then, for higher temperatures, the combustion phenomenon is divided into two main regions, *first* (FC) and *second combustion* (SC). These intervals were separated according to the thermal event close to 400°C, clearly observed in the temperature profile. The total consumption of asphaltenes is carried out at the end of SC. Each region is defined by a particular behavior associated with its mass change and mass change rate curves at the time of its decomposition in mathematical functions (conventionally Gaussian/Lorentzian), which perfectly describe the area under the DTG curve [16, 55, 56, 80, 84].

Then, the effect of pressure was evaluated on n-C_7 asphaltene oxidation. The results are shown in Fig. 5.5. Panels a–c show the rate for mass change and panels d–f the mass change profiles for pressures between 0.084 MPa to 6.0 MPa. According to the results, asphaltene oxidation is a pressure-dependent phenomenon, due to both profiles being modified with the increase in pressure [85–87]. For atmospheric pressure, the asphaltene profile is divided into low- and high-temperature regions. Contrasting, pressures higher than 0.3 MPa modify the oxidation behavior from 2 to 4 thermal events.

In the current context, panels a–c of the same figure shows that pressure generates a positive effect on asphaltene oxidation reflected in the number and intensity peaks of the rate for mass change. In panel a, a single peak is observed close to 450°C, which is in accordance with results reported for asphaltene oxidation at low pressures [88]. By contrast, in panels b and c, two peaks appear at 380°C and 450°C. Besides, a slight elevation is observed around 300°C. The lowers temperature peaks in the rate for mass change of asphaltene oxidation seem to arise from DCO and FC thermal events. On the other hand, panels d–f show that OC and DCO do not occur at low pressure since an increase in sample mass is not obtained for low

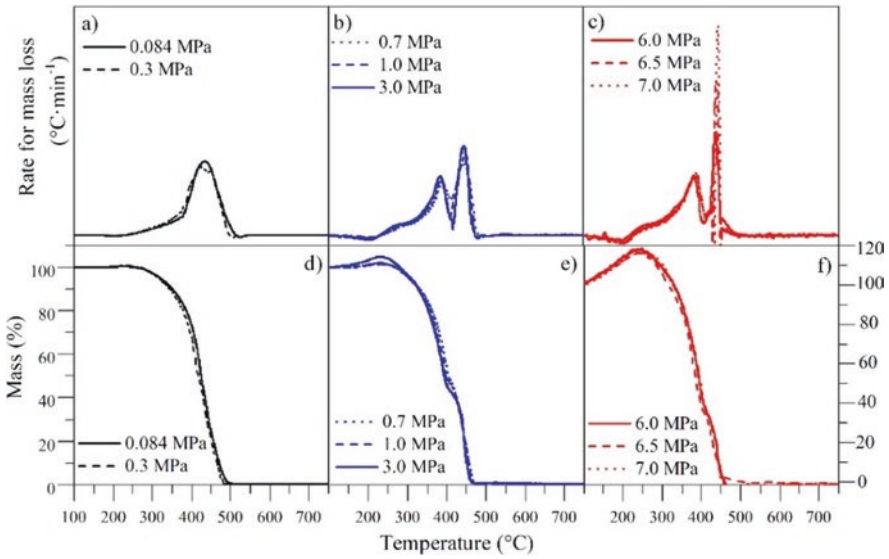

Fig. 5.5 (**a**–**c**) Rate for mass loss and (**d**–**f**) mass percentage for *n*-C_7 asphaltene oxidation at different pressures between 0.084 MPa and 7.0 MPa. Heating rate, 10°C·min^{-1}; airflow, 80 mL·min^{-1}; and sample mass, 1 mg. (Taken with permission from Medina et al. [73])

temperatures. These results suggest that oxygen chemisorption plays a vital role in asphaltene oxidation since the molecules become more reactive; hence there is an easy bond scission. Besides, the volatile content is driven off at lower temperatures [88]. The oxidation of heavy hydrocarbon structures occurs in the most reactive sites, i.e., peripherical molecules and heteroatoms.

Also, the basal plane of the aromatic structure could promote oxygen anchorage [8]. High-pressure's main effects promote the probability of oxygen atoms collision and, hence, higher kinetic energy [89, 90]. During SC the solid product obtained after FC is characterized for a low H/C ratio, high polarity, and aromaticity degree, since aliphatic structures react during DCO and FC regions, promoting aromatic condensation degree.

5.7.3.2 Thermo-Oxidation of Different N-C_7 Asphaltenes

The effect of the chemical nature of asphaltene over its oxidation was evaluated using six different asphaltene sources. Samples were named as A, B, C, D, E, and F asphaltenes. The thermograms were constructed at three different pressures (0.084 MPa, 3.0 MPa, and 6.0 MPa). Figure 5.6 shows the mass change and rate for mass change profiles for the systems evaluated.

Results show that the oxidation process depends directly on the asphaltene chemical structure and the increment of pressure remarks on the differences between the rate for mass change and mass change profiles. For all systems, asphaltene

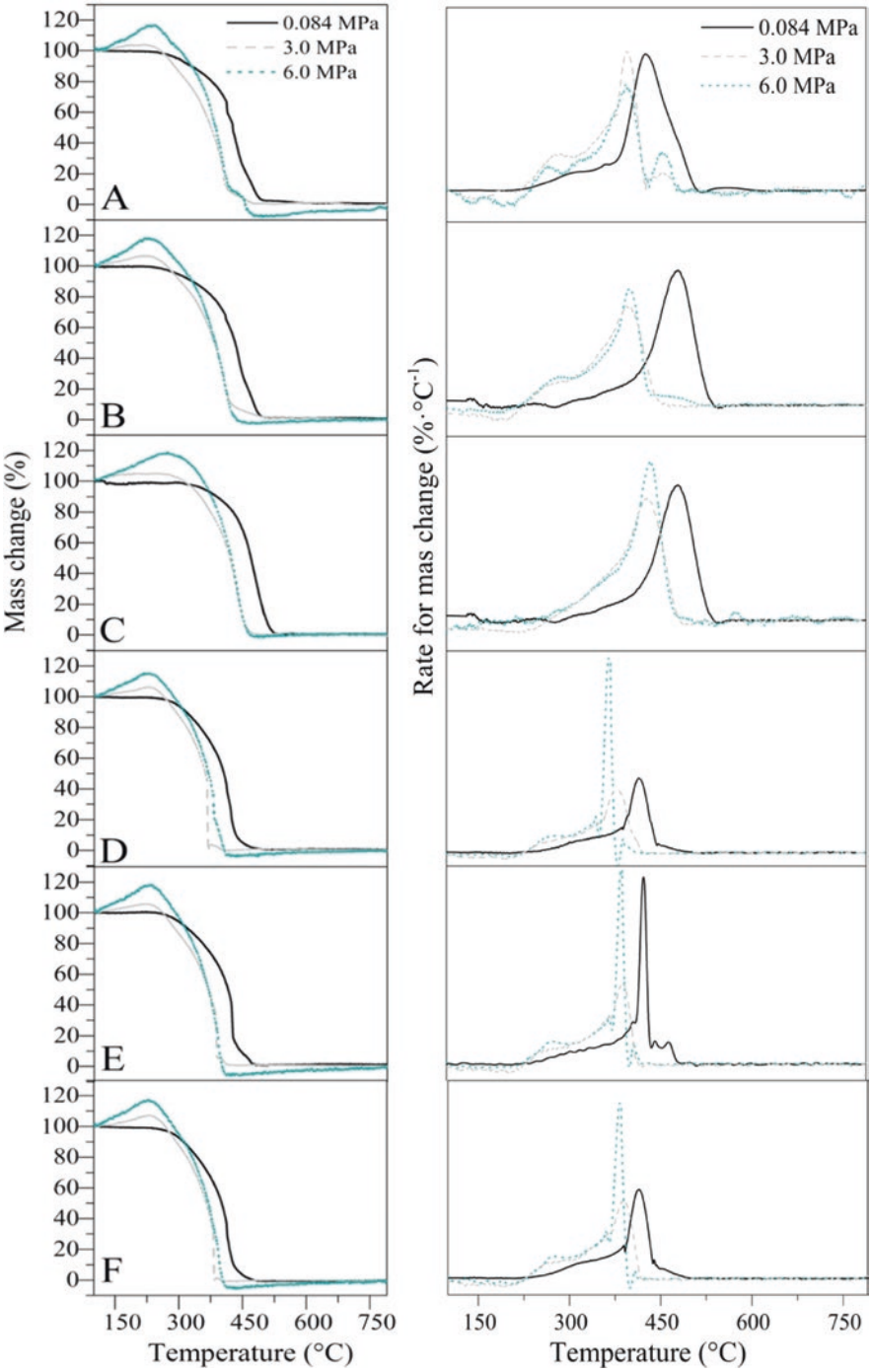

Fig. 5.6 Mass percentage and rate for mass change for different n-C_7 asphaltene oxidations at different pressures from 0.084 MPa to 6.0 MPa. Sample weight, 1 mg; heating rate, 10°C·min^{-1}; and airflow, 80 mL·min^{-1}. (Taken with permission from Medina et al. [67])

decomposition is defined by four thermal events as described in the previous section, for pressures higher than 3.0 MPa [91]. According to mass change profiles, oxygen chemisorption degree increases following the trend D < F < E < B < A < C. Substantial differences in the amount of oxygen chemisorbed in each sample can be associated with the amount of free radicals, heteroatoms, aromaticity degree, and diameter of clusters and aggregates. Free radicals vary according to the asphaltene source, between 10^{15} and 10^{20} spins·g^{-1}. The greater the amount of free radicals, the greater the chemisorption of oxygen [92]. Besides, the increase in pressure promotes an increase in oxygen chemisorbed percentage due to aggregates' thermal expansion [93]. A direct relationship between the content of carbonyl and carboxyl functional groups was found. Despite the increase in oxygen content following the order E ≈ F < D < A ≈ B < C, the amount of these functional groups increases as follows D < F < E < B < A < C, which agrees with OC%. Carboxyl groups are characterized by their easiness for being ionized by hydrogen proton releasing from OH^- group [94]; therefore oxygen is strongly activated in these active sites. On the other hand, according to ^{1}H-NMR results reported in previous work [67], the increase in aromatization degree and the decrease in alkylation degree favor the anchorage of oxygen molecules on asphaltene structure. As the number of fused rings in the polyaromatic core increases, the intermolecular interactions increase too [95]. Therefore, the formation of ketones, phenols, ethers, and alcohols takes place [91]. It has been reported that at low temperatures (100–150°C), ketones and aromatic ethers are the main oxygenated functional groups in asphaltene structures [92].

According to X-ray diffraction analysis, reported in previous work [67], the decrease in the cluster's diameter increases the mass gained in the OC region, because there is a bigger surface area/volume ratio for oxygen anchorage, added to the asphaltene molecular expansion by pressure effect.

DCO region also is favored by high-pressure systems, as the loss of mass increases in the order 3.0 MPa < 6.0 MPa. This is obtained for all samples. Between asphaltenes, the mass loss percentage increases in the order D < F < E < C < B < A. The samples with higher OC increment lost a higher mass in the DCO region. It implies that in effect during DCO occurs mainly the decomposition of the oxygenated structures, which at the same time are more reactive [91]. Besides, X-ray photoelectron spectroscopy analysis shows the influence of the different functional groups. Samples with the highest thioether content have shown the highest mass loss in DCO. This sulfur form is characterized to require low energy for oxidizing. Besides the position on saturated structure facilitates their decomposition at low temperatures [96]. As for 1H-NMR, according to the *H*α values, it was also found that a high content of methyl, ethyl, and methylene structures promotes a greater loss of mass in DCO region [97].

For combustion regions, the chemical nature of asphaltenes considerably influences the FC and SC behavior at high-pressure conditions. The asphaltenes with a high content of short aliphatic chains and heteroatoms located in branched structures decompose around 70% of their mass. According to the asphaltenes' initial composition, the remaining coke after this region will have a different composition due to the loss of peripheral substituents [98] and the ability to create steric

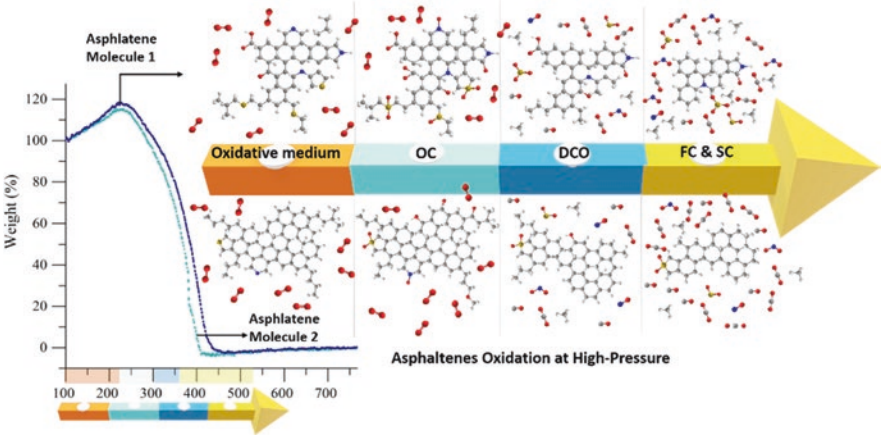

Fig. 5.7 Representative diagram for different n-C_7 asphaltene oxidations at high-pressure conditions. (Taken with permission from Medina et al.)

hindrance and prevent polyaromatic condensation [98]. This was corroborated by XRD results, where samples with high intensity for γ-band and low intensity for (002)-bands have favorable conditions for polyaromatic sheets stacked together to produce coke [99]. Hence, during SC, for samples with low content of aliphatic structures and high aromatic degree, a high amount of asphaltenes is required to decompose, independently of system pressure. In the current context, aromatic functional groups, including thiophenes, pyrroles, and pyridines, also promote a higher mass loss in SC, adding extra polar interactions between the aromatic structures [100]. Figure 5.7 shows the differences in the profiles obtained from two asphaltene molecules with different functional groups, different sizes of the aromatic nucleus, and different molecular weights, among others.

5.7.3.3 Thermocatalytic Oxidation of N-C_7 Asphaltenes

SS asphaltenes were selected to evaluate the effect of different nanocatalysts on asphaltene oxidation at high- and low- pressure conditions. Figure 5.8 shows the results in mass change and rate for mass change for asphaltene oxidation with (a) support, (b) 3:1AuPd, and (c) 10:1AuPd nanocatalysts at non-isothermal conditions. According to the profiles obtained, the presence of nanocatalysts maintains the decomposition of asphaltenes defined by 4 thermal events for pressures greater than 1.0 MPa, i.e., 0.7 MPa higher than in the absence thereof. This suggests that a more significant mass diffusion occurs for virgin molecules at lower pressures [101]. The mixed support shows an important reduction in asphaltene decomposition for all pressure evaluations. The inclusion of Zr^{4+} on the internal molecular structure of ceria improves their catalytic activity by the increment in oxygen storage capacity, directly related to redox reactions. As reported in the literature, the

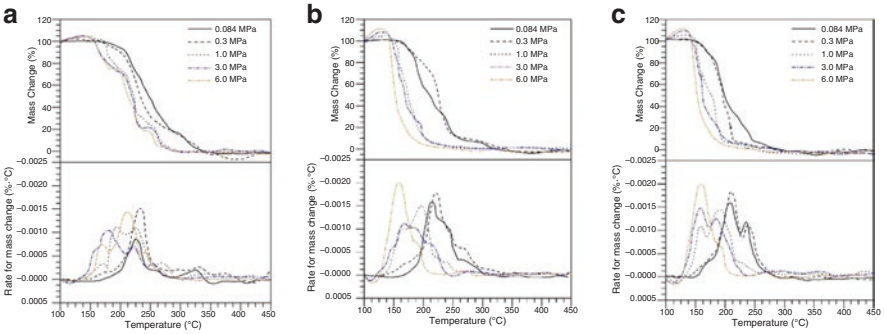

Fig. 5.8 Mass in percentage and rate for mass change for *n*-C_7 asphaltene oxidation in the presence and absence of bi-elemental catalysts 3:1AuPd and 10:1AuPd at different pressures from 0.084 MPa to 6.0 MPa. Sample weight, 1 mg; *n*-C_7 asphaltene load, 0.2 mg·m^{-2}; heating rate, 10°C·min^{-1}; and airflow, 80 mL·min^{-1}. (Taken with permission from Medina et al. [83])

couple Ce3+/C4+ plays an important role in asphaltene decomposition, being the main mechanism for hydrogen production in cracking processes. By using nanocatalysts, the oxygen chemisorbed decreases considerably at 6.0 MPa; however, the reactivity of samples is favored by this event, ending the total decomposition for the systems with higher OC%. Lower pressures present a higher OC% for adsorbed than virgin asphaltenes. For DCO region, nanocatalysts cause most of the asphaltene to decompose in this region at lower temperatures (< 230°C). Nevertheless, for lower pressures, the mass loss is equally distributed in the three decomposition regions. This is corroborated by the rate for mass change peaks. For low-pressure systems, the main decomposition peak is observed at 230°C, but pressures higher than 1.0 MPa show an increase in intensity peak at 160°C.

As literature reports, active sites on the support surface can improve the catalytic activity of the materials. In this study, two noble elements (Au and Pd) were used in different nominal ratios (10:1 and 3:1). From results, it is appreciated that similar to support, the four thermal events remain for high-pressure systems. Nevertheless, substantial differences in intensity and temperature peaks are obtained in each system [102]. Comparing with support, both functionalized nanocatalysts improve the oxidation behavior of asphaltenes by increasing oxygen chemisorption percentage, reduction of temperature peaks, and increase in intensity peaks at low temperatures and therefore its reduction at high temperatures. Besides, pressure increases improve the catalytic behavior of AuPd-based nanocatalysts. For lower pressures, the peak at 200°C and 190°C is predominant for 3:1AuPd and 10:1AuPd, respectively. These temperatures are reduced as pressure goes up, achieving 170°C and 160°C at 6.0 MPa for the same systems.

Oxygen chemisorption was higher for nanocatalysts with a higher amount of Au active phases (i.e., 10:1AuPd). Interactions between oxygen from the environment and noble elements favor the oxygen transfer to asphaltene molecules by spillover mechanism [103, 104]. In the current context, the DCO region is also favored in the same nanocatalyst trend described. As the carbonaceous molecules become oxygen-rich during OC, in DCO they lose a higher amount of mass. For example, 10: AuPd

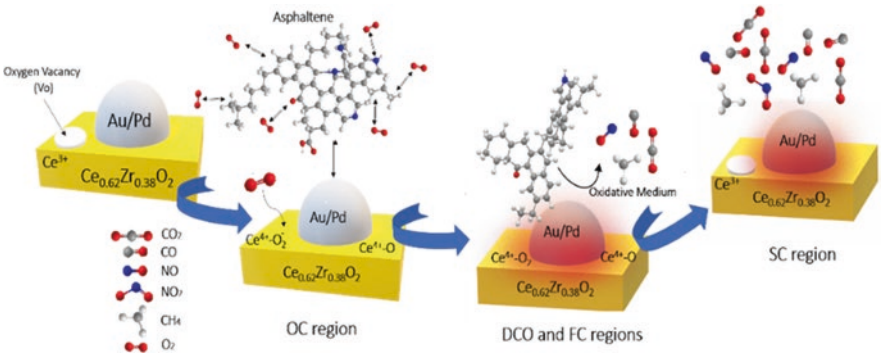

Fig. 5.9 Schematic illustration for thermocatalytic oxidation of n-C_7 asphaltenes using AuPd/$Ce_{0.62}Zr_{0.38}O_2$ nanocatalysts discretized in the four thermal regions. (Taken with permission from Medina et al. [83])

and 3:1AuPd lost 90% and 80% of the initial mass, respectively, during DCO zone at 6.0 MPa. In this sense, during FC and SC, the asphaltene mass loss is considerably reduced for high-pressure systems.

In addition, according to surface nanocatalysts characterization, the influence of different ions on asphaltene catalytic activity was found. High Pd^{2+} ions concentration promotes a detriment in catalytic activity, while Ce^{3+} and Au^0 increase the reactivity of the materials under the operational conditions. These results indicate that nanocatalysts require a good design based on structural and phase complexity for selective oxidation of asphaltenes [61, 105].

Figure 5.9 shows mechanistic insights about the catalytic oxidation process of n-C_7 asphaltene oxidation over bi-elemental nanocatalysts.

Figure 5.9 tries to present the main mechanisms that act in the decomposition of asphaltenes at high pressure. First, the adsorption of asphaltenes occurs mainly in the active phases of the noble elements. Simultaneously, with increasing temperature, the oxygen molecules adsorb onto the oxygen anion vacancies on the surface of the support (OC region). Here, oxidation of asphaltenes occurs during the OC region. When nanocatalysts acquire enough energy, the first oxygenated fractions decompose during DCO, a redox cycle takes place, and the first gaseous products are formed, including sulfur-, nitrogen-, and oxygen-based gases. Finally, at the end of the FC region, a solid with a high condensed and aromatic degree is obtained due to the loss of aliphatic chains. In SC, the total decomposition of the condensed molecules is generated.

5.7.4 Estimation of Kinetic Parameters

5.7.4.1 Asphaltene Oxidation at Different Pressures

The effective activation energy for SS asphaltenes oxidation was calculated for all systems at different pressure conditions, discretizing the total phenomenon in four thermal events. Plotting $\ln\left[\beta\left(-\ln\left(1-x\right)\right)\times\left(\mathrm{P}_{O_2}T^2\right)^{-1}\right]$ against $1{\cdot}T_i^{-1}$ and using the

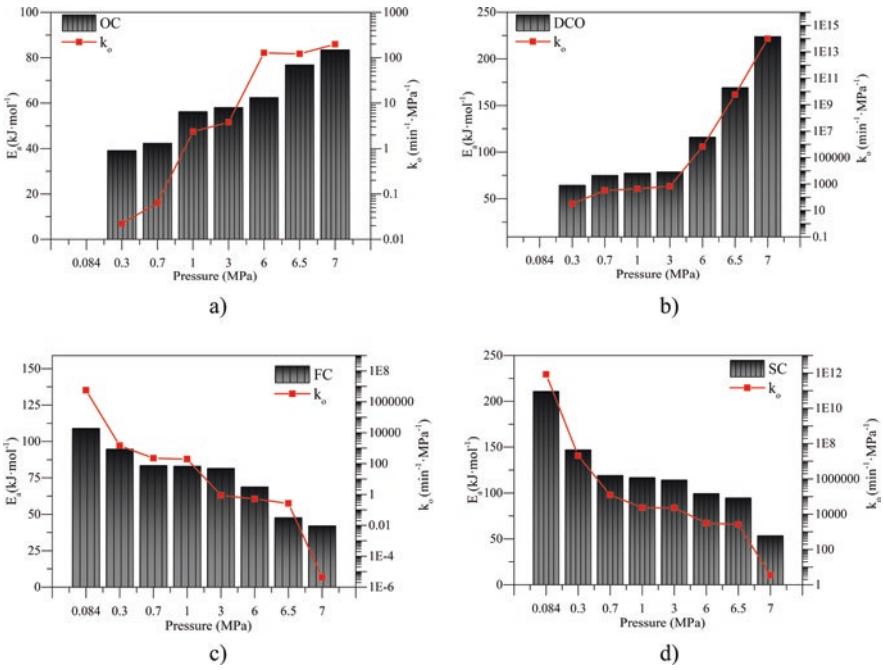

Fig. 5.10 Estimated kinetic parameters for *n*-C_7 asphaltene oxidation at different pressures discretized in different regions, including (**a**) oxygen chemisorption (OC), (**b**) decomposition of the chemisorbed oxygen (DCO) region, (**c**) first combustion (FC) region, and (**d**) second combustion (SC) region. (Results taken from Medina et al. [91])

slope and intercept of the straight line, E_a and k_o are obtained, respectively. Results are shown in Fig. 5.10 a–d. As temperature was divided into shorter intervals, a first-order reaction fits decomposition profiles correctly with $R^2 > 0.99$.

From panel (a) of Fig. 5.10, it is observed that E_a increases as pressure increases. Values vary between 39.12 kJ·mol^{-1} and 83.46 kJ·mol^{-1} in the pressure range evaluated. The amount of chemisorbed oxygen increases considerably for high-pressure systems; the energy to carry out this process also increases.

This same trend is followed for the DCO thermal event. Because with the increase in pressure, there are a greater number of oxygen structures formed, there is a greater energy expenditure in their decomposition.

Effective activation energies for DCO are higher than for the OC region, varying between 64.47 kJ·mol^{-1} and 223.84 kJ·mol^{-1}. Finally, for the combustion regions, the activation energy at lower pressures is higher than in DCO; however, for high pressures, FC and SC have lower values, due to the high degree of decomposed structures during DCO, and high conversion degree implies high activation energy values.

For the Arrhenius pre-exponential factor, it is observed dependency on the pressure system. Pressure modifies k_o values by several orders of magnitude [91]. As the number of accessible number states increases, Arrhenius values during OC are

varied due to the change in entropy change by the system's molecular disorganization and the formation of an activated complex.

5.7.4.2 Kinetic Analysis for Different N-C_7 Asphaltenes at High-Pressure Conditions

Kinetic analysis was done for the n-C_7 asphaltenes from different sources. Figure 5.11 shows the results obtained. From panels a–b, it is observed an increase in E_a during OC and DCO region as pressure increases for all samples. As it was

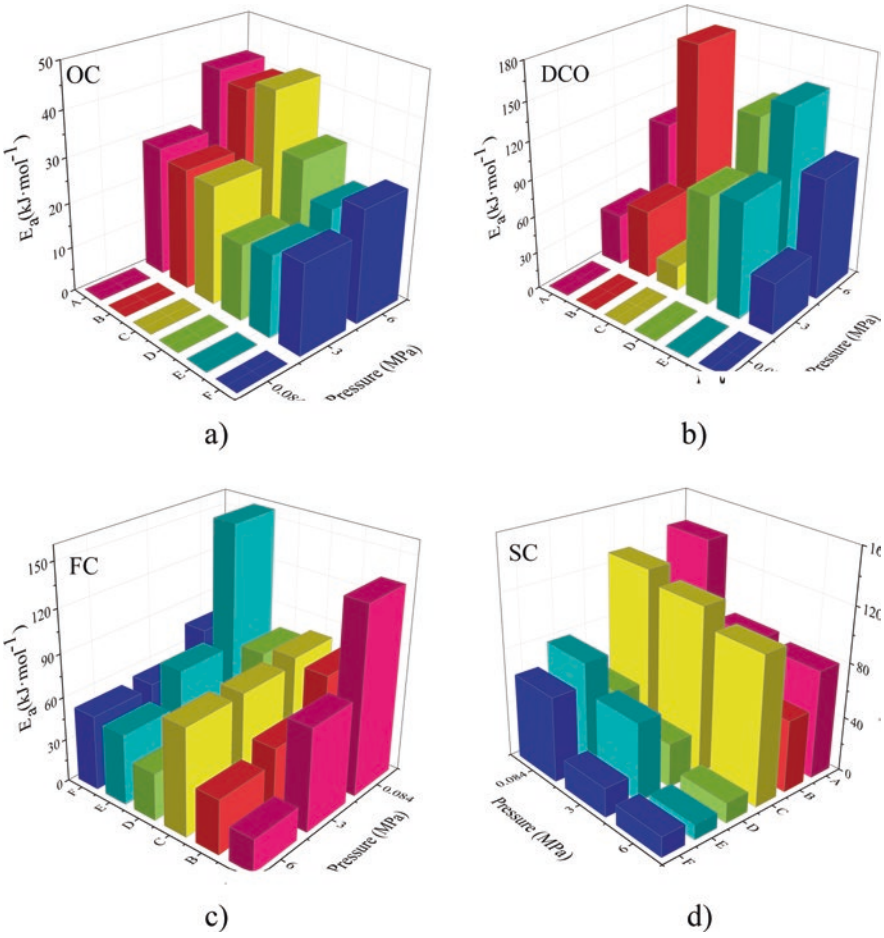

Fig. 5.11 Estimated effective activation energy for the oxidation of different n-C_7 at 0.084 MPa, 3.0 MPa, and 6.0 MPa discretized in different regions including (*a*) oxygen chemisorption (OC), (*b*) decomposition of the chemisorbed oxygen (DCO) region, (*c*) first combustion (FC) region, and (*d*) second combustion (SC) region. (Results are taken from Medina et al. [67])

explained, DCO depends on the functional groups formed during OC zone. Regardless of the chemical nature of asphaltene, by increasing pressure, the number of oxygenated structures increases, due to interactions with free radicals, heteroatoms, and aromatic rings, among others. Each asphaltene has different active sites for oxygen anchorage, and pressure favors this phenomenon in all cases [91, 106, 107]. On the other hand, the differences in E_a values between each sample are directly related to its chemical nature and origin. Samples with a higher aromatic degree show a higher activation energy value. Functional nitrogen and sulfur groups also affect these results. Aromatic nitrogen and sulfur reduce activation energy. The opposite is obtained for carboxyl and carbonyl groups. The high content of these groups increases the activation energy.

The values of E_a during DCO are higher than the obtained for OC, which is in accordance with the results previously exposed [91, 108]. Nevertheless, pressure generates a positive effect over asphaltene oxidation since the energy required to complete combustion zones is reduced.

On the other hand, asphaltenes with a smaller cluster size present lower E_a values during FC. This is due to the breakdown of alkyl side chains, making the asphaltenes more refractory at the end of this region. Finally, in SC region, several chemical reactions occur, including dealkylation/cyclization of aliphatic chains, combination/polymerization/condensation and peri-condensation of aromatic rings, and aromatization of naphthenic rings, mainly in asphaltenes like A, B, and C, reflected in their higher values for effective activation energy [9, 86, 109].

5.7.4.3 Kinetic Analysis for N-C_7 Asphaltene Catalytic Oxidation

Kinetic study was done for thermocatalytic oxidation of *n*-C_7 asphaltene based on effective activation energy. The values for both parameters are shown in Fig. 5.12. From results, it is appreciated that according to the chemical nature of nanocatalysts, E_a presents significant differences. The effect of pressure in the presence of nanocatalysts is the same as for virgin asphaltenes. Pressure increment implies higher energy values for OC and DCO thermal events and lower values for combustion zones. Besides, nanocatalysts with higher catalytic activity show higher energy values for OC and DCO regions. Contrasting with virgin asphaltenes, the adsorbed molecules reduces the activation energy around 17 kJ·mol^{-1} for the best system (10:1AuPd). This result could be associated with a faster consumption of heavy oil fraction in the active sites when increasing the system pressure [110–113]. As mentioned, DCO follows the same trend because higher energy is required to complete the decomposition of the oxygenated compounds. Nevertheless, due to the high mass loss during this region caused by the materials' catalytic activity, the E_a values for these systems are higher than for free asphaltenes. This increase is offset by the decrease in E_a for FC and SC events. Functionalized materials show the highest reduction in these thermal events related to the synergic effect between noble metals and ceria-zirconia support.

In all systems, both the chemical nature of the nanocatalyst and the system pressure changes the kinetic parameter values. For the case of pressure, it favors the global kinetic rate for *n*-C_7 asphaltene oxidation reactions, independently of the asphaltene source.

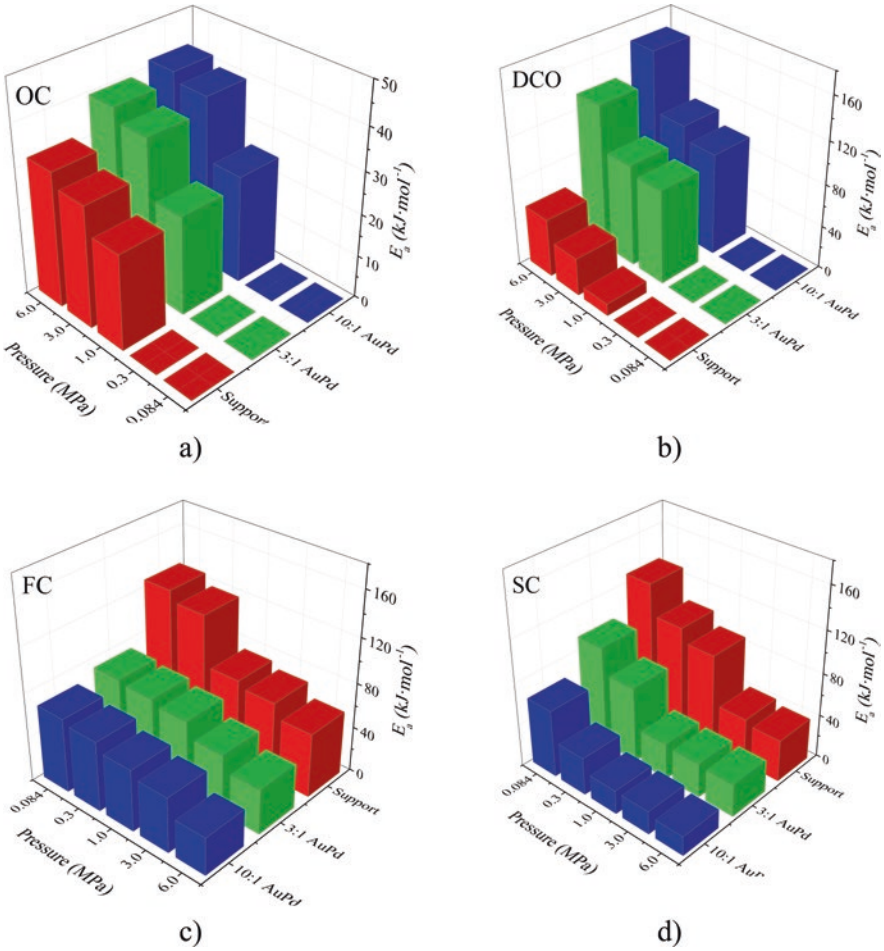

Fig. 5.12 Estimated effective activation energy for n-C_7 asphaltene oxidation with different nanocatalysts. Discretized in the different regions including (**a**) oxygen chemisorption (OC), (**b**) decomposition of the chemisorbed oxygen (DCO) region, (**c**) first combustion (FC) region, and (**d**) second combustion (SC) region. (Results are taken from Medina et al. [83])

5.7.5 Compensation Effect

5.7.5.1 Compensation Effect on N-C_7 Asphaltene Oxidation at Different Pressures

Figure 5.13 shows the experimentally measured effective activation energy (E_a) and ln(k_o) values for asphaltene oxidation discretized in different thermal regions known as oxygen chemisorption (OC), desorption of chemisorbed oxygen functional groups (DCO), first combustion (FC), and second combustion (SC), at pressures between 0.084 MPa and 7.0 MPa. A linear compensation effect (dotted line) was observed between E_a and ln(k_o). Standard deviations of 3.0%, 2.0%, 4.0%, and 5.0% were obtained for activation energy during OC, DCO, FC, and SC, respectively,

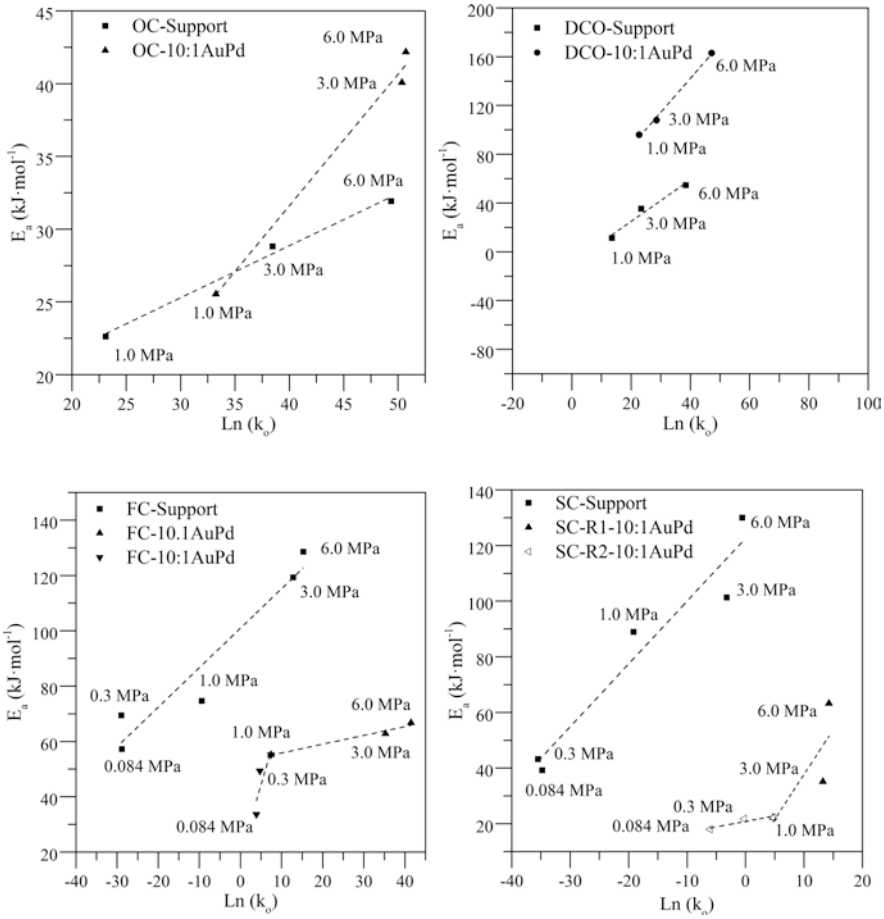

Fig. 5.13 Dependence of effective activation energy E_a on the logarithm of the Arrhenius pre-exponential factor k_o for asphaltene oxidation under different pressure conditions from 0.084 MPa to 7.0 MPa and different heating rates (HR) from 5°C·min^{-1} to 15°C·min^{-1}, divided into the four thermal events OC, DCO, FC, and SC. R# means the number of mechanisms of reaction to take control of each thermal event during asphaltene oxidation at different pressures

while ln(k_o) presents deviations lower than 3.0% in all regions. Many efforts have been made to explain several processes' thermodynamic compensation effect [114, 115]. It has been argued that large statistical uncertainties are associated with the nature of Arrhenius's law, due to the experimental determination of the kinetic parameters (i.e., E_a and k_o), and therefore, a compensatory effect is achieved [114, 116]. According to Fig. 5.1, the DCO, FC, and SC phenomena show a direct relationship between the E_a and ln(k_o) values. Unlike these, during OC, there is a variation in the linearity of this trend with the increase in pressure.

This result indicates that there are variations on the linear dependence of apparent activation energy and pre-exponential factor attributed to the number of ways in

which the heat can provide the energy needed to overcome the barrier to carry out the asphaltene oxidation at low temperatures with system pressure increases. This behavior indicates that entropy and enthalpy of activation are linearly related to each stage's activation energy, making evident the occurrence of a compensation effect in different stages [116]. In this zone, the oxidant's initiation likely proceeds by hydrogen abstraction, and the subsequent reaction of the asphaltene radicals can either lead to oxygen incorporation [117]. This corroborates the two mechanisms suggested by the compensation effect to carry out OC.

For the development of the DCO, FC, and SC regions, in the initial stage, the asphaltene decomposition was done along a reaction path with high activation energy and with relatively high negative values of ΔS^{T} due to the nature of the labile oxides in the new molecular (asphaltene*) oxygenated structure [118]. Therefore, there is a high value of k_o when E_a is high (i.e., for pressures >0.7 MPa). Although the same trend was observed in FC regarding DCO, lower activation energy values were obtained. During FC occurs the loss of aliphatic functional groups, dissociation of heteroatoms positioned in branched structures [119, 120], leading to a weaker interaction between the molecules and an almost unimolecular reaction with a relatively low ΔS^{T} negative value [118]. For low values of E_a, pre-exponential factor values are greatly reduced. At the end of this region, the asphaltene molecules change from a flaccid to a tight structure. Again, high E_a values are found, characteristic of the decomposition of the heaviest solid residue after the decomposition of the lightest groups in the asphaltene structure [120]. The increase of k_o makes a positive effect on the rate constant, compensated by the E_a increment, with a negative contribution to the rate constant.

5.7.5.2 Compensation Effect for Oxidation of N-C_7 Asphaltenes in the Presence of Nanocatalysts at Different Pressures

Figure 5.14 shows the effective activation energy as a function of $\ln(k_o)$ for asphaltene oxidation in the presence of support and AuPd-supported nanocatalysts between 0.084 MPa and 6.0 MPa. Results were presented according to the four thermal events that describe the asphaltene decomposition curves under high-pressure conditions. Throughout the results, it was identified as a linear correlation between the E_a values and $\ln(k_o)$ for a reaction developed at different pressures. This means that an increase of the reaction rate (i.e., the increment of the frequency factor) can be compensated with a rise in the E_a (and therefore reaction rate decrease), as system pressure changes. All experiments in which each nanocatalysts is involved fit to a single line with good correlation, suggesting that asphaltenes react under the same mechanism through the same intermediates as pressure is modified. However, between each nanocatalyst, two independent lines were obtained. In ceria-zirconia mixed oxide, oxygen chemisorption is controlled by oxygen activated by the functional groups of support and gas phase, known as lattice oxygen [121, 122]. Some research suggest that the main mechanism for asphaltene decomposition on ceria-based nanocatalysts is determined by the redox cycle (Ce^{4+}/Ce^{3+}) [51, 52, 123], and

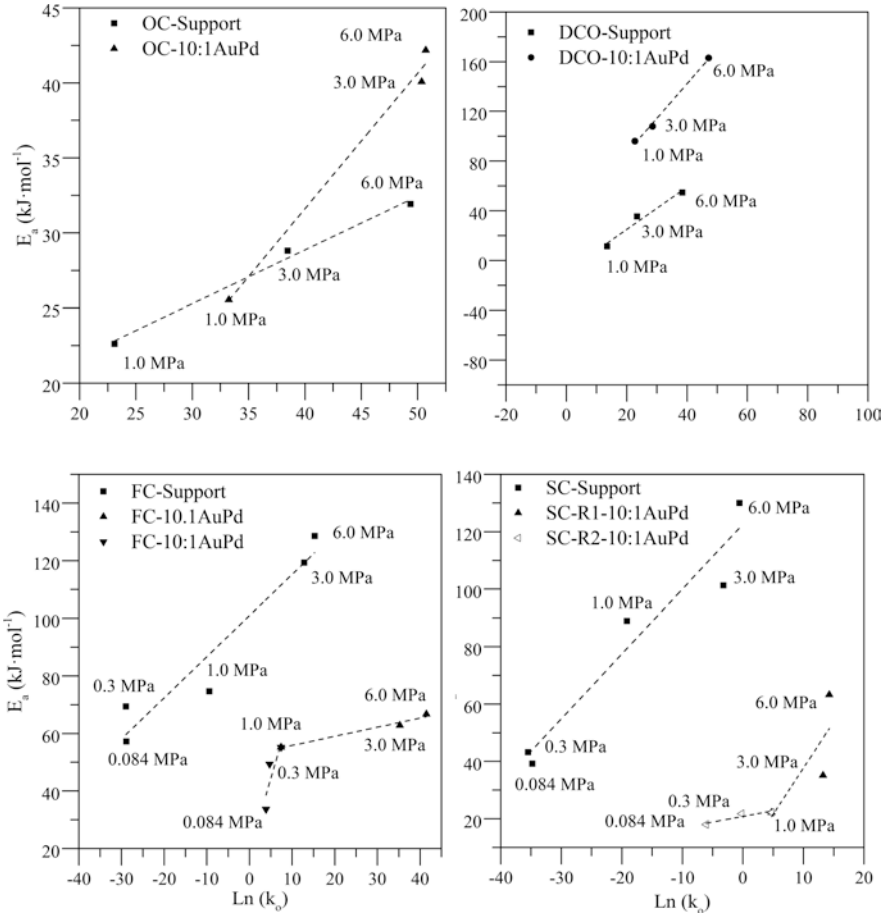

Fig. 5.14 Dependence of activation energy E_a on the logarithm of the pre-exponential factor k_o for the oxidation of nanoparticles containing asphaltenes under different pressure conditions from 0.084 MPa to 6.0 MPa, divided into the four thermal events OC, DCO, FC, and SC. R# means the number of mechanisms of reaction to take control in each thermal event during asphaltene oxidation at different pressures

the inclusion of isovalent and aliovalent Zr^{4+} on ceria fluorite structure improves the oxygen storage and hence the capability to reduce Ce^{4+} to Ce^{3+} [61, 105]. On the contrary, the incorporation of active phases of Pd and Au element oxides on the surface of ceria-zirconia mixed oxide modifies the asphaltene oxidation mechanism [124]. Oxygen chemisorption exists in the form of Au-O, Au = O, Au-O-Au, Pd = O, Pd-O-Pd, and Pd-O, being these phases more active and reactive for oxidation reactions [103, 104]. Compensation effect is attributed to the different activation energy associated with the heterogeneity of the surface, whose relative number is modified with pressure variations, also varying the adsorption capacity of reactants and products. These results show the importance of determining the structural complexity of

nanocatalysts for selective asphaltene oxidation. For example, the effective activation energy to create a surface oxygen vacancy in the upper oxygen layer of ceria-based materials is less on the surface of doped mixed oxide ($AuPd/Ce_{0.62}Zr_{0.38}O_2$) than it is on pure oxide.

DCO also shows that there are no changes in the global mechanism for asphaltene decomposition by varying the pressure as a linear dependency of activation energy against $\ln(k_o)$ was observed. Both variables vary in parallel ways. Nevertheless, according to the different chemical natures of each system, different reaction pathways are founded, following to the transition state theory (TST) for heterogeneous reactions [125, 126]. TST suggests that the concentration of the active sites plays a key role in the rate constant, showing a direct relationship. Hence, the changes in activation energy have been attributed to enthalpies' founded modifications on the different surfaces provided by Au, Pd, Ce, and Zr element oxides. For combustion FC and SC regions, two different pathways were found for 10:1AuPd nanocatalysts due to the heterogeneous surface and the different catalytic powers of each phase. At low pressures, there is another mechanism for asphaltene decomposition than at high pressures. This result corroborates the hypothesis that during OC the asphaltene structure is modified and its reactivity changes.

The addition of nanocatalysts does not change the trend of k_o and E_a during combustion zones. High values of the pre-exponential factor imply high values of effective activation energy. During FC, decomposition of groups occurs after the detachment of the oxygen groups in DCO, which are not as heavy as those that decompose in SC. This event is associated with low negatives values for ΔS^{T}. The opposite behavior is observed in SC, with the highest values for k_o and E_a. Hence, the change in compensation effect suggests a change in reaction mechanism, which strongly depends on the physicochemical properties of the nanocatalysts.

5.8 Conclusion

This work was focused on understanding the effect of pressure over the thermo-oxidation behavior of asphaltenes with and without nanocatalyst. Both thermo-oxidation and thermocatalytic oxidation of asphaltene showed a direct dependence on the system temperature and pressure. Unlike the results at low pressure, asphaltenes undergo marked oxidation at low temperatures when the system pressure is greater than 0.7 MPa and 1.0 MPa for virgin and adsorbed asphaltenes, respectively. The effective activation energy values using $AuPd/Ce_{0.62}Zr_{0.38}O_2$ nanocatalyst was reduced by more than 30% for all the pressures evaluated. Moreover, according to the distributed activation energy models, the decomposition of asphaltenes occurs in several simultaneous reactions of order n = 1 due to the multiple mechanisms involved in asphaltene oxidation/decomposition and molecular complexity.

Besides, it was found that the pressure follows the compensation effect for asphaltene mass loss in the presence and absence of nanocatalysts. Oxygen

chemisorption, a dominant event at high pressures and low temperatures, follows two different reaction mechanisms: hydrogen abstraction and free radical reactions. In the case of nanocatalysts, it has been suggested that the distribution of active sites with varying reactivity could explain the compensation effect. Here, it was found that each catalyst follows a global reaction mechanism as the pressure is changed. Despite that the asphaltene oxidation in the presence and absence of nanocatalysts follows the compensation effect with changes in the system pressure, a marked change in the OC region was observed, where the reaction pathway goes from two global mechanisms to one for the *n*-C_7 asphaltenes with and without nanocatalyst, respectively.

Compensation effect plots are useful to evaluate if the reaction pathway is changing by the change of any experimental variable, such as T, P, catalyst, and the molecular structure of the reagents (asphaltenes for this case), among others.

Acknowledgments The authors would like to acknowledge the Universidad Nacional de Colombia for their financial and logistical support.

References

1. O.E. Medina Erao, J. Gallego, C.M. Olmos, X. Chen, F.B. Cortés, C.A. Franco, Effect of multifunctional Nanocatalysts on n-C7 Asphaltene adsorption and subsequent oxidation under high pressure conditions. Energy Fuel (2020)
2. D.W. Green, G.P. Willhite, *Enhanced oil recovery* vol. 6: Henry L. Doherty Memorial Fund of AIME, Society of Petroleum Engineers Richardson, TX, (1998)
3. S. Thomas, Enhanced oil recovery-an overview. Oil & Gas Science and Technology-Revue de l'IFP **63**, 9–19 (2008)
4. T. Nasr, G. Beaulieu, H. Golbeck, G. Heck, Novel expanding solvent-SAGD process "ES-SAGD", in *Canadian International Petroleum Conference*, (2002)
5. P.A. Govind, S.K. Das, S. Srinivasan, T.J. Wheeler, Expanding solvent SAGD in heavy oil reservoirs, in *International Thermal Operations and Heavy Oil Symposium*, (2008)
6. A.-Y. Huc, *Heavy crude oils: from geology to upgrading: an overview*. Editions Technip, (2010)
7. X.-G. Dong, Q.-F. Lei, W.-J. Fang, Q.-S. Yu, Thermogravimetric analysis of petroleum asphaltenes along with estimation of average chemical structure by nuclear magnetic resonance spectroscopy. Thermochim. Acta **427**, 149–153 (2005)
8. P. Murugan, T. Mani, N. Mahinpey, K. Asghari, The low temperature oxidation of Fosterton asphaltenes and its combustion kinetics. Fuel Process. Technol. **92**, 1056–1061 (2011)
9. N.P. Freitag, Chemical-reaction mechanisms that govern oxidation rates during in-situ combustion and high-pressure air injection. SPE Reserv. Eval. Eng. **19**, 645–654 (2016)
10. X. Zhang, Q. Liu, Z. Fan, Enhanced in situ combustion of heavy crude oil by nickel oxide nanoparticles. Int. J. Energy Res. **43**, 3399–3412 (2019)
11. N.N. Nassar, A. Hassan, P. Pereira-Almao, Clarifying the catalytic role of NiO nanoparticles in the oxidation of asphaltenes. Appl. Catal. A Gen. **462**, 116–120 (2013)
12. M.M. Husein, S.J. Alkhaldi, In situ preparation of alumina nanoparticles in heavy oil and their thermal cracking performance. Energy Fuel **28**, 6563–6569 (2014)
13. F. Amin, A study on the adsorption and catalytic oxidation of Asphaltene onto nanoparticles. J. Pet. Sci. Technol. **7**, 21–29 (2017)

14. A. Amrollahi Biyouki, N. Hosseinpour, N.N. Nassar, Pyrolysis and oxidation of Asphaltene-born coke-like residue formed onto in situ prepared NiO nanoparticles toward advanced in situ combustion enhanced oil recovery processes. Energy Fuel **32**, 5033–5044 (2018)
15. A.A. Akhmadiyarov, I.T. Rakipov, A.A. Khachatrian, A.A. Petrov, S.A. Sitnov, A.V. Gerasimov, et al., Thermocatalytic upgrading of heavy oil by iron oxides nanoparticles synthesized by oil-soluble precursors. J. Pet. Sci. Eng. **169**, 200–204 (2018)
16. C.A. Franco, T. Montoya, N.N. Nassar, P. Pereira-Almao, F.B. Cortés, Adsorption and subsequent oxidation of colombian asphaltenes onto nickel and/or palladium oxide supported on fumed silica nanoparticles. Energy Fuel **27**, 7336–7347 (2013)
17. J. Barillas, T.D. Júnior, W. Mata, Improved oil recovery process for heavy oil: A review. Brazilian Journal of Petroleum and Gás **2** (2008)
18. J. Burger, P. Sourieau, M. Combarnous, H.J. Ramey, *Thermal methods of oil recovery*: Gulf Publishing Company, Book Division, (1985)
19. J. Alvarez, S. Han, Current overview of cyclic steam injection process. Journal of Petroleum Science Research **2** (2013)
20. P.S. Sarathi and D.K. Olsen, Practical aspects of steam injection processes: A handbook for independent operators, National Inst. for Petroleum and Energy Research, Bartlesville, OK, (1992)
21. M. Cokar, I.D. Gates, M.S. Kallos, Reservoir simulation of steam fracturing in early-cycle cyclic steam stimulation. SPE Reserv. Eval. Eng. **15**, 676–687 (2012)
22. Q. Jiang, B. Thornton, J. Russel-Houston, S. Spence, Review of thermal recovery technologies for the Clearwater and lower grand rapids formations in the cold lake area in Alberta. J. Can. Pet. Technol. **49**, 2–13 (2010)
23. R. Butler, C. Yee, Progress in the in situ recovery of heavy oils and bitumen. J. Can. Pet. Technol. **41** (2002)
24. J.C. de Souza Jr, D.F. Cursino, K.G. Padua, Twenty Years of Vapor Injection in Heavy-Oil Fields, in *SPE Latin American and Caribbean Petroleum Engineering Conference*, (2005)
25. E. Hanzlik, D. Mims, Forty years of steam injection in California-The evolution of heat management, in *SPE International Improved Oil Recovery Conference in Asia Pacific*, (2003)
26. D.W. Zhao, J. Wang, I.D. Gates, Thermal recovery strategies for thin heavy oil reservoirs. Fuel **117**, 431–441 (2014)
27. D.W. Zhao, J. Wang, I.D. Gates, An evaluation of enhanced oil recovery strategies for a heavy oil reservoir after cold production with sand. Int. J. Energy Res. **39**, 1355–1365 (2015)
28. A.J. Rosa, R. de Souza Carvalho, J.A.D. Xavier, *Engenharia de reservatórios de petróleo*: Interciência, (2006)
29. R. Butler, A new approach to the modelling of steam-assisted gravity drainage. J. Can. Pet. Technol. **24**, 42–51 (1985)
30. R. Butler, D. Stephens, The gravity drainage of steam-heated heavy oil to parallel horizontal wells. J. Can. Pet. Technol. **20** (1981)
31. L. Yang, D.-S. Zhou, Y.-h. Sun, SAGD as follow-up to cyclic steam stimulation in a medium deep and extra heavy oil reservoir, in *International Oil & Gas Conference and Exhibition in China*, (2006)
32. J. Jimenez, The field performance of SAGD projects in Canada, in *International petroleum technology conference*, (2008)
33. I. Gates, N. Chakrabarty, Optimization of steam-assisted gravity drainage in McMurray reservoir, in *Canadian International Petroleum Conference*, (2005)
34. S. Akin, S. Bagci, A laboratory study of single-well steam-assisted gravity drainage process. J. Pet. Sci. Eng. **32**, 23–33 (2001)
35. V. Alvarado, E. Manrique, Enhanced oil recovery: An update review. Energies **3**, 1529–1575 (2010)
36. C. Chu, A study of fireflood field projects (includes associated paper 6504). J. Pet. Technol. **29**, 111–120 (1977)

37. C. Cheih, State-of-the-art review of fireflood field projects (includes associated papers 10901 and 10918). J. Pet. Technol. **34**, 19–36 (1982)
38. A. Turta, S. Chattopadhyay, R. Bhattacharya, A. Condrachi, W. Hanson, Current status of commercial in situ combustion projects worldwide. J. Can. Pet. Technol. **46** (2007)
39. C. Wu, P. Fulton, Experimental simulation of the zones preceding the combustion front of an in-situ combustion process. Soc. Pet. Eng. J. **11**, 38–46 (1971)
40. L. Castanier, W. Brigham, Upgrading of crude oil via in situ combustion. J. Pet. Sci. Eng. **39**, 125–136 (2003)
41. N. Mahinpey, A. Ambalae, K. Asghari, In situ combustion in enhanced oil recovery (EOR): A review. Chem. Eng. Commun. **194**, 995–1021 (2007)
42. A.I. El-Diasty, A.M. Aly, Understanding the mechanism of nanoparticles applications in enhanced oil recovery, in *SPE North Africa Technical Conference and Exhibition*, (2015)
43. C.A. Franco, N.N. Nassar, M.A. Ruiz, P. Pereira-Almao, F.B. Cortés, Nanoparticles for inhibition of asphaltenes damage: Adsorption study and displacement test on porous media. Energy Fuel **27**, 2899–2907 (2013)
44. S. Mokhatab, M.A. Fresky, M.R. Islam, Applications of nanotechnology in oil and gas E&P. J. Pet. Technol. **58**, 48–51 (2006)
45. A.I. El-Diasty, A.M.S. Ragab, Applications of nanotechnology in the oil & gas industry: Latest trends worldwide & future challenges in Egypt, in *North Africa Technical Conference and Exhibition*, (2013)
46. F. Ariza, C. Andrés, Synthesis and application of supported metallic and multi-metallic oxides nanoparticles for in-situ upgrading and inhibition of formation damage, Ph.D. Thesis, Universidad Nacional de Colombia-Sede Medellín, Online, (2015)
47. N.N. Nassar, C.A. Franco, T. Montoya, F.B. Cortés, A. Hassan, Effect of oxide support on Ni–Pd bimetallic nanocatalysts for steam gasification of n-C7 asphaltenes. Fuel **156**, 110–120 (2015)
48. D. López, L.J. Giraldo, J.P. Salazar, D.M. Zapata, D.C. Ortega, C.A. Franco, et al., Metal oxide nanoparticles supported on macro-mesoporous Aluminosilicates for catalytic steam gasification of heavy oil fractions for on-site upgrading. Catalysts **7**, 319 (2017)
49. T. Montoya, B.L. Argel, N.N. Nassar, C.A. Franco, F.B. Cortés, Kinetics and mechanisms of the catalytic thermal cracking of asphaltenes adsorbed on supported nanoparticles. Pet. Sci. **13**, 561–571 (2016)
50. O.E. Medina, J. Gallego, D. Arias-Madrid, F.B. Cortés, C.A. Franco, Optimization of the load of transition metal oxides (Fe2O3, Co3O4, NiO and/or PdO) onto CeO2 nanoparticles in catalytic steam decomposition of n-C7 Asphaltenes at low temperatures. Nano **9**, 401 (2019)
51. O.E. Medina, J. Gallego, L.G. Restrepo, F.B. Cortés, C.A. Franco, Influence of the Ce4+/Ce3+ redox-couple on the cyclic regeneration for adsorptive and catalytic performance of NiO-PdO/CeO2±δ nanoparticles for n-C7 asphaltene steam gasification. Nano **9**, 734 (2019)
52. O.E. Medina, Y. Hurtado, C. Caro-Velez, F.B. Cortés, M. Riazi, S.H. Lopera, et al., Improvement of steam injection processes through nanotechnology: An approach through in situ upgrading and foam injection. Energies **12**, 4633 (2019)
53. C. Franco, E. Patiño, P. Benjumea, M.A. Ruiz, F.B. Cortés, Kinetic and thermodynamic equilibrium of asphaltenes sorption onto nanoparticles of nickel oxide supported on nanoparticulated alumina. Fuel **105**, 408–414 (2013)
54. L. Cardona Rojas, Efecto de nanopartículas en procesos con inyección de vapor a diferentes calidades, Msc Magister Thesis, Universidad Nacional de Colombia-Sede Medellín, Online, 2018
55. N.N. Nassar, A. Hassan, P. Pereira-Almao, Comparative oxidation of adsorbed asphaltenes onto transition metal oxide nanoparticles. Colloids Surf. A Physicochem. Eng. Asp. **384**, 145–149 (2011)
56. N.N. Nassar, A. Hassan, P. Pereira-Almao, Effect of surface acidity and basicity of aluminas on asphaltene adsorption and oxidation. J. Colloid Interface Sci. **360**, 233–238 (2011)

57. N.N. Nassar, A. Hassan, L. Carbognani, F. Lopez-Linares, P. Pereira-Almao, Iron oxide nanoparticles for rapid adsorption and enhanced catalytic oxidation of thermally cracked asphaltenes. Fuel **95**, 257–262 (2012)
58. N.N. Nassar, A. Hassan, G. Vitale, Comparing kinetics and mechanism of adsorption and thermo-oxidative decomposition of Athabasca asphaltenes onto TiO2, ZrO2, and CeO2 nanoparticles. Appl. Catal. A Gen. **484**, 161–171 (2014)
59. C.A. Franco, M.M. Lozano, S. Acevedo, N.N. Nassar, F.B. Cortés, Effects of resin I on Asphaltene adsorption onto nanoparticles: A novel method for obtaining asphaltenes/resin isotherms. Energy Fuel **30**, 264–272 (2015)
60. M.M. Lozano, C.A. Franco, S.A. Acevedo, N.N. Nassar, F.B. Cortés, Effects of resin I on the catalytic oxidation of n-C 7 asphaltenes in the presence of silica-based nanoparticles. RSC Adv. **6**, 74630–74642 (2016)
61. C.M. Olmos, L.E. Chinchilla, J.J. Delgado, A.B. Hungría, G. Blanco, J.J. Calvino, et al., CO oxidation over bimetallic au–Pd supported on ceria–zirconia catalysts: Effects of oxidation temperature and au: Pd molar ratio. Catal. Lett. **146**, 144–156 (2016)
62. L. Barre, D. Espinat, E. Rosenberg, M. Scarsella, Colloidal structure of heavy crudes and asphaltene solutions. Revue de l'Institut Français du Pétrole **52**, 161–175 (1997)
63. A. International, ASTM D5236–13, Standard Test Method for Distillation of Heavy Hydrocarbon Mixtures (Vacuum Potstill Method), *Annual Book of ASTM Standards,* (2013)
64. A. International, ASTM D2892, Standard Test Method for Distillation of Crude Petroleum (15-Theoretical Plate Column), *Annual Book of ASTM Standards,* (2016)
65. S.M. Lopes, P. Geng, Estimation of elemental composition of diesel fuel containing biodiesel. SAE International Journal of Fuels and Lubricants **6**, 668–676 (2013)
66. S. Acevedo, J. Castillo, V. Vargas, A. Castro, O.Z. Delgado, C.A.F. Ariza, et al., Suppression of phase separation as a hypothesis to account for nuclei or nanoaggregate formation by Asphaltenes in toluene. Energy Fuel (2018)
67. O.E. Medina, J. Gallego, N.N. Nassar, S.A. Acevedo, F.B. Cortés, C.A. Franco, Thermo-oxidative decomposition Behaviors of different sources of n-C7 Asphaltenes at high-pressure conditions. Energy Fuel (2020)
68. C. Lee, W. Yang, R.G. Parr, Results obtained with the correlation energy density functionals. Phys. Rev. B: Condens. Matter Mater. Phys **37**, 785 (1988)
69. H.L. Schmider, A.D. Becke, Optimized density functionals from the extended G2 test set. J. Chem. Phys. **108**, 9624–9631 (1998)
70. O.C. Mullins, Optical interrogation of aromatic moieties in crude oils and Asphaltenes, in *Structures and Dynamics of Asphaltenes*, ed. by O. C. Mullins, E. Y. Sheu, (Springer, Boston, MA, 1998). https://doi.org/10.1007/978-1-4899-1615-0_2
71. S. Goncalves, J. Castillo, A. Fernandez, J. Hung, Absorbance and fluorescence spectroscopy on the aggregation behavior of asphaltene–toluene solutions. Fuel **83**, 1823–1828 (2004)
72. N.N. Nassar, A. Hassan, P. Pereira-Almao, Application of nanotechnology for heavy oil upgrading: Catalytic steam gasification/cracking of asphaltenes. Energy Fuel **25**, 1566–1570 (2011)
73. O.E. Medina, J. Gallego, E. Rodríguez, C.A. Franco, F.B. Cortés, Effect of pressure on the oxidation kinetics of Asphaltenes. Energy Fuel **33**, 10734–10744 (2019)
74. O. Talu, F. Meunier, Adsorption of associating molecules in micropores and application to water on carbon. AICHE J. **42**, 809–819 (1996)
75. T. Montoya, D. Coral, C.A. Franco, N.N. Nassar, F.B. Cortés, A novel solid–liquid equilibrium model for describing the adsorption of associating asphaltene molecules onto solid surfaces based on the "chemical theory". Energy Fuel **28**, 4963–4975 (2014)
76. G.-S. Liu, S. Niksa, Coal conversion submodels for design applications at elevated pressures. Part II. Char gasification. Prog. Energy Combust. Sci. **30**, 679–717 (2004)
77. P. Schneider, Adsorption isotherms of microporous-mesoporous solids revisited. Appl. Catal. A Gen. **129**, 157–165 (1995)

78. M. Kurian, C. Kunjachan, Effect of lattice distortion on physical properties and surface morphology of nanoceria framework with incorporation of iron/zirconium. Nano-Structures & Nano-Objects **1**, 15–23 (2015)
79. A.E.E. Shilov, *Activation of Saturated Hydrocarbons by Transition Metal Complexes*, vol 5 (Springer Science & Business Media, 1984)
80. C.A. Franco-Ariza, J.D. Guzmán-Calle, F.B. Cortés-Correa, Adsorption and catalytic oxidation of asphaltenes in fumed silica nanoparticles: Effect of the surface acidity. Dyna **83**, 171–179 (2016)
81. F.B. Cortés, T. Montoya, S. Acevedo, N.N. Nassar, C.A. Franco, Adsorption-desorption of n-c7 asphaltenes over micro-and nanoparticles of silica and its impact on wettability alteration. CT&F-Ciencia, Tecnología y Futuro **6**, 89–106 (2016)
82. C.A. Franco, T. Montoya, N.N. Nassar, F.B. Cortés, NiO and PdO supported on Fumed silica nanoparticles for adsorption and catalytic steam gasification of Colombian n-C7 Asphaltenes. Handbook on Oil Production Research **26**, 101–145 (2014)
83. O.E. Medina, J. Gallego, C.M. Olmos, X. Chen, F.B. Cortés, C.A. Franco, Effect of multifunctional nanocatalysts on n-C7 Asphaltene adsorption and subsequent oxidation under high-pressure conditions. Energy & Fuels (2020) 2020/03/29
84. N.N. Nassar, A. Hassan, G. Luna, P. Pereira-Almao, Kinetics of the catalytic thermo-oxidation of asphaltenes at isothermal conditions on different metal oxide nanoparticle surfaces. Catal. Today **207**, 127–132 (2013)
85. O. Sonibare, R. Egashira, T. Adedosu, Thermo-oxidative reactions of Nigerian oil sand bitumen. Thermochim. Acta **405**, 195–205 (2003)
86. P. Murugan, N. Mahinpey, T. Mani, Thermal cracking and combustion kinetics of asphaltenes derived from Fosterton oil. Fuel Process. Technol. **90**, 1286–1291 (2009)
87. P.R. Herrington, Effect of concentration on the rate of reaction of asphaltenes with oxygen. Energy Fuel **18**, 1573–1577 (2004)
88. N. Hosseinpour, Y. Mortazavi, A. Bahramian, L. Khodatars, A.A. Khodadadi, Enhanced pyrolysis and oxidation of asphaltenes adsorbed onto transition metal oxides nanoparticles towards advanced in-situ combustion EOR processes by nanotechnology. Appl. Catal. A Gen. **477**, 159–171 (2014)
89. P. Hänggi, P. Talkner, M. Borkovec, Reaction-rate theory: Fifty years after Kramers. Rev. Mod. Phys. **62**, 251 (1990)
90. B.J. Berne, M. Borkovec, J.E. Straub, Classical and modern methods in reaction rate theory. J. Phys. Chem. **92**, 3711–3725 (1988)
91. O.E. Medina, J. Gallego, E. Rodriguez, C.A. Franco, F.B. Cortés, Effect of pressure on the oxidation kinetics of Asphaltenes. Energy Fuel (2019)
92. N.M. Sánchez, A. de Klerk, Low-temperature oxidative asphaltenes liquefaction for petrochemicals: Fact or fiction? Appl. Petrochem. Res. **6**, 97–106 (2016)
93. M. Gonçalves, M. Teixeira, R. Pereira, R. Mercury, J.D.R. Matos, Contribution of thermal analysis for characterization of asphaltenes from Brazilian crude oil. J. Therm. Anal. Calorim. **64**, 697–706 (2001)
94. D. Kuakpetoon, Y.-J. Wang, Structural characteristics and physicochemical properties of oxidized corn starches varying in amylose content. Carbohydr. Res. **341**, 1896–1915 (2006)
95. B.E. Ascanius, D.M. Garcia, S.I. Andersen, Analysis of asphaltenes subfractionated by N-methyl-2-pyrrolidone. Energy Fuel **18**, 1827–1831 (2004)
96. Y.B. Bava, M. Geronés, L.J. Giovanetti, L. Andrini, M.F. Erben, Speciation of Sulphur in asphaltenes and resins from Argentinian petroleum by using XANES spectroscopy. Fuel **256**, 115952 (2019)
97. F.S. AlHumaidan, A. Hauser, M.S. Rana, H.M. Lababidi, NMR characterization of Asphaltene derived from residual oils and their thermal decomposition. Energy Fuel **31**, 3812–3820 (2017)
98. O.C. Mullins, The modified yen model. Energy Fuel **24**, 2179–2207 (2010)

99. N.T. Nguyen, K.H. Kang, C.W. Lee, G.T. Kim, S. Park, Y.-K. Park, Structure comparison of asphaltene aggregates from hydrothermal and catalytic hydrothermal cracking of C5-isolated asphaltene. Fuel **235**, 677–686 (2019)
100. I. Fernandez, G. Frenking, Direct estimate of conjugation and aromaticity in cyclic compounds with the EDA method. Faraday Discuss. **135**, 403–421 (2007)
101. A. Martínez-Arias, M. Fernández-García, C. Belver, J. Conesa, J. Soria, EPR study on oxygen handling properties of ceria, zirconia and Zr–Ce (1: 1) mixed oxide samples. Catal. Lett. **65**, 197–204 (2000)
102. O.E. Medina, C. Olmos, S.H. Lopera, F.B. Cortés, C.A. Franco, Nanotechnology applied to thermal enhanced oil recovery processes: A review. Energies **12**, 4671 (2019)
103. C.M. Olmos, L.E. Chinchilla, E.G. Rodrigues, J.J. Delgado, A.B. Hungría, G. Blanco, et al., Synergistic effect of bimetallic au-Pd supported on ceria-zirconia mixed oxide catalysts for selective oxidation of glycerol. Appl. Catal. B Environ. **197**, 222–235 (2016)
104. U.S. Ozkan, R.B. Watson, The structure–function relationships in selective oxidation reactions over metal oxides. Catal. Today **100**, 101–114 (2005)
105. C.F. Zinola, Carbon monoxide oxidation assisted by interfacial oxygen-water layers. J. Solid State Electrochem. **23**, 883–901 (2019)
106. O. Senneca, N. Vorobiev, A. Wütscher, F. Cerciello, S. Heuer, C. Wedler, et al., Assessment of combustion rates of coal chars for oxy-combustion applications. Fuel **238**, 173–185 (2019)
107. S. Niksa, G.-S. Liu, R.H. Hurt, Coal conversion submodels for design applications at elevated pressures. Part I. devolatilization and char oxidation. Prog. Energy Combust. Sci. **29**, 425–477 (2003)
108. A. Zahabi, M.R. Gray, T. Dabros, Kinetics and properties of asphaltene adsorption on surfaces. Energy Fuel **26**, 1009–1018 (2012)
109. V. Calemma, P. Iwanski, M. Nali, R. Scotti, L. Montanari, Structural characterization of asphaltenes of different origins. Energy Fuel **9**, 225–230 (1995)
110. G. Duffy, L. Morpeth, A. Cousins, D. Roberts, J. Edwards, Investigation of the effect of total pressure on performance of the catalytic water–gas shift reaction using simulated coal-derived syngases. Catal. Commun. **11**, 272–275 (2009)
111. G. Chinchen, R. Logan, M. Spencer, Water-gas shift reaction over an iron oxide/chromium oxide catalyst.: II: Stability of activity. Appl. Catal. **12**, 89–96 (1984)
112. G. Chinchen, R. Logan, M. Spencer, Water-gas shift reaction over an iron oxide/chromium oxide catalyst.: I: Mass transport effects. Appl. Catal. **12**, 69–88 (1984)
113. K. Atwood, M. Arnold, E. Appel, Water-gas shift reaction. Effect of pressure on rate over an Iron-oxide-chromium oxide catalyst. Industrial & Engineering Chemistry **42**, 1600–1602 (1950)
114. C.A. Bennett, R.S. Kistler, K. Nangia, W. Al-Ghawas, N. Al-Hajji, A. Al-Jemaz, Observation of an isokinetic temperature and compensation effect for high-temperature crude oil fouling. Heat Transfer Engineering **30**, 794–804 (2009)
115. A.K. Galwey, M. Mortimer, Compensation effects and compensation defects in kinetic and mechanistic interpretations of heterogeneous chemical reactions. Int. J. Chem. Kinet. **38**, 464–473 (2006)
116. G. Gottstein, L. Shvindlerman, The compensation effect in thermally activated interface processes. Interface Science **6**, 267–278 (1998)
117. R. Javadli, A. de Klerk, Desulfurization of heavy oil–oxidative desulfurization (ODS) as potential upgrading pathway for oil sands derived bitumen. Energy Fuel **26**, 594–602 (2012)
118. K. Czajka, A. Kisiela, W. Moroń, W. Ferens, W. Rybak, Pyrolysis of solid fuels: Thermochemical behaviour, kinetics and compensation effect. Fuel Process. Technol. **142**, 42–53 (2016)
119. B. Wei, P. Zou, X. Zhang, X. Xu, C. Wood, Y. Li, Investigations of structure–property–thermal degradation kinetics alterations of Tahe Asphaltenes caused by low temperature oxidation. Energy Fuel **32**, 1506–1514 (2018)

120. W. Zijun, L. Wenjie, Q. Guohe, Q. Jialin, Structural characterization of gudao asphaltene by ruthenium ion catalyzed oxidation. Pet. Sci. Technol. **15**, 559–577 (1997)
121. C. Li, Q. Xin, Spillover and migration of surface species on catalysts, in *Proceedings of the 4th International Conference on Spillover*, (1997), p. 18
122. K. Fujimoto, Catalyst design based on spillover theory, in *Studies in Surface Science and Catalysis*, vol. 77, (Elsevier, 1993), pp. 9–16
123. O.E. Medina, C. Caro-Vélez, J. Gallego, F.B. Cortés, S.H. Lopera, C.A. Franco, Upgrading of extra-heavy crude oils by dispersed injection of NiO–PdO/CeO2±δ Nanocatalyst-based Nanofluids in the steam. Nano **9**, 1755 (2019)
124. F. Buciuman, F. Patcas, T. Hahn, A spillover approach to oxidation catalysis over copper and manganese mixed oxides. Chem. Eng. Process. Process Intensif. **38**, 563–569 (1999)
125. J.R. Alvarez-Idaboy, N. Mora-Diez, A. Vivier-Bunge, A quantum chemical and classical transition state theory explanation of negative activation energies in OH addition to substituted ethenes. J. Am. Chem. Soc. **122**, 3715–3720 (2000)
126. W.C. Conner Jr., A general explanation for the compensation effect: The relationship between ΔS‡ and activation energy. J. Catal. **78**, 238–246 (1982)